Wave-Induced Motion and Drag Reduction of Kelp

Jayde Fanjieh Meng[1] and Marcelo Chamecki[2]

[1]Stanford University
[2]University of California, Los Angeles

November 8, 2023

Abstract

It is well known that the motion of flexible vegetation leads to drag reduction in comparison to rigid vegetation. In this study, we use a numerical model to investigate how the detailed motion of kelp fronds in response to forcing by surface gravity waves can impact the drag exerted by the kelp on waves. We find that this motion can be characterized in terms of three dimensionless numbers: (1) the ratio of hydrodynamic drag to buoyancy, (2) the ratio of blade length to wave excursion, and (3) the Keulegan-Carpenter number, which measures the ratio of drag to inertial forces. We quantify drag reduction, and find that inertial forces can significantly impact the amplitude of kelp motion and amount of kelp drag reduction. Under certain wave conditions, inertial forces can cause kelp fronds to accelerate more quickly relative to the wave, which can lead to increased drag reduction and reduced wave energy dissipation. In some conditions, frond motion leads to drag augmentation in comparison to rigid fronds. Additionally, we discuss other features of kelp motion, such as the degree of asymmetry, and their relationship with enhanced drag reduction.

Wave-Induced Motion and Drag Reduction of Kelp

Jayde F. Meng[1], **Marcelo Chamecki**[1]

[1]Department of Atmospheric and Oceanic Sciences, University of California, Los Angeles, CA 90025, USA

Key Points:

- A 2D parameter space is proposed to characterize dominant forces and classify different types of kelp motion
- Inertial forces can significantly impact frond motion and drag reduction, and even lead to drag augmentation (compared to rigid fronds)
- We provide empirical fits to quantify drag reduction/augmentation in low- and high-inertia conditions

Corresponding author: Marcelo Chamecki, chamecki@ucla.edu

Abstract

It is well known that the motion of flexible vegetation leads to drag reduction in comparison to rigid vegetation. In this study, we use a numerical model to investigate how the detailed motion of kelp fronds in response to forcing by surface gravity waves can impact the drag exerted by the kelp on waves. We find that this motion can be characterized in terms of three dimensionless numbers: (1) the ratio of hydrodynamic drag to buoyancy, (2) the ratio of blade length to wave excursion, and (3) the Keulegan-Carpenter number, which measures the ratio of drag to inertial forces. We quantify drag reduction, and find that inertial forces can significantly impact the amplitude of kelp motion and amount of kelp drag reduction. Under certain wave conditions, inertial forces can cause kelp fronds to accelerate more quickly relative to the wave, which can lead to increased drag reduction and reduced wave energy dissipation. In some conditions, frond motion leads to drag augmentation in comparison to rigid fronds. Additionally, we discuss other features of kelp motion, such as the degree of asymmetry, and their relationship with enhanced drag reduction.

Plain Language Summary

We use a numerical model to study how kelp fronds move in response to passing ocean waves. Flexible motion reduces the drag forces experienced by the kelp and increases survival in extreme conditions such as energetic waves. Frond motion also reduces the amount of wave energy dissipation. The type of motion that the fronds undergo in response to different types of waves is determined by the dominant forces, and so is the amount of drag reduction. Our findings show that, unlike other types of aquatic vegetation, inertial forces (e.g. due to the pressure variations in the water) can be as important as (and sometimes more important) than the drag forces caused by the flow.

1 Introduction

Macroalgae species, such as kelp, are integral to the health of many coastal ecosystems. Kelp forests help preserve biodiversity by serving as habitats and food sources for different marine species (Dayton et al., 1984; Schiel & Foster, 2015). Kelp forests also help remediate anthropogenic changes, by mitigating eutrophication pollution through nitrate removal (Gao et al., 2021) and reducing ocean acidification and offsetting carbon dioxide emissions via carbon sequestration (Froehlich et al., 2019; Hoegh-Guldberg et al., 2019). Globally, kelp forests generate an average of $500 billion a year in terms of ecosystem services (Eger et al., 2023).

Moreover, kelp harvesting is central to numerous local economies. Many cultures around the world have a rich history of relying on kelp as a food source, a way to enhance fisheries, a fertilizer for soil, etc. (Thornton, 2015; Kain & Dawes, 1987). More recently, alginate sourced from kelp has also been utilized as an important additive in pharmaceutical and biomedical industries (Peteiro, 2018). Furthermore, the high energy content and fast growth rates of kelp have singled them out to be a potential source of biofuel that does not compete for space with land-grown crops for the food industry (Milledge et al., 2014; Frieder et al., 2022).

With all of these benefits, it is critical to understand how we can sustainably support the growth and maintenance of kelp forests and farms. In particular, we are interested in the hydrodynamic interactions between kelp and ocean waves. This study focuses primarily on the hydrodynamics of the kelp species *Macrocystis pyrifera*, more commonly known as giant kelp. Giant kelp is native to the coasts of California and is particularly well-suited for the purposes of farming due to its fast growth rates (up to 0.5 meters per day). They are the largest species of algae and can reach lengths of 20 meters or more (Abbott & Hollenberg, 1992).

This type of kelp is made up of dozens of fronds attached to a holdfast, which keeps the kelp anchored to the substrate. Each frond consists of a stem-like stipe and leaf-like blades, and at the base of each blade is a pneumatocyst, or a gas-filled bladder. These pneumatocysts allow *M. pyrifera* to be highly buoyant. Giant kelp stipes also have relatively low rigidity compared to seagrasses, allowing stipes to easily bend in response to hydrodynamic forces. A diagram of kelp physiology is given in Fig. 1(a).

Many past observational studies on *M. pyrifera* (henceforth simply referred to as kelp) hydrodynamics have focused on quantifying the bulk effects of kelp on the flow. The drag force imparted by the kelp on the currents reduces flow rates through kelp forests (Jackson & Winant, 1983; Gaylord et al., 2007). For example, Monismith et al. (2022) estimated the scaling for kelp forest drag coefficient in tidal flows via biomass relationships. Laboratory studies have also shown that the presence of kelp modifies wave orbital velocities (Rosman et al., 2013). However, kelp forests generally dissipate minimum amounts of wave energy due to its highly flexible nature (Elwany et al., 1995).

Because of its nearshore environment, kelp are especially sensitive to the forces caused by surface gravity waves (Gaylord et al., 2003). High energy wave amplitudes can cause kelp stipes to break and entangle, or even dislodge fronds from their holdfast (Seymour et al., 1989; Dayton et al., 1984). Kelp fronds have also been observed to respond differently to waves with different periods (Mullarney & Pilditch, 2017). Generally, flexibility is a strategy employed by seagrasses and algae to reduce drag forces and increase survivability in high-flow environments (Vogel, 1984; Utter & Denny, 1996). In return, the drag exerted on the waves by kelp is highly dependent on the detailed motion of the kelp frond. Thus, the two-way interaction between flexible kelp fronds and waves impact both, the survivability of kelp and the physical properties of the waves.

Numerical models have also been used to predict the forces that individual kelp fronds undergo in different wave conditions, and thus, how likely they are to survive. For example, Jackson and Winant (1983) modeled kelp stipes as rigid vertical columns, while Utter and Denny (1996) represented kelp fronds as buoys attached to a flexible rope and predicted kelp survivability rates under different wave conditions. They model a single point element where hydrodynamic forces such as buoyancy, drag, and pressure gradient forces are countered by tension (Utter & Denny, 1996; Denny et al., 1997).

Additionally, a number of more sophisticated numerical models have been developed to investigate submerged aquatic vegetation motion under wave conditions, including but not limited to variations of the Euler-Bernoulli beam model utilized by Marjoribanks et al. (2014), Zeller et al. (2014), and Luhar and Nepf (2016). Zhu et al. (2020) expanded on this work and developed a consistent-mass cable model to study asymmetric motion of aquatic vegetation. However, these models have not been applied to the study of giant kelp, in part because they suffer from numerical stability issues in cases with low bending stiffness (Zeller et al., 2014).

A major thrust of theoretical and numerical studies is to develop understanding and quantification of how plant motion affects drag reduction. For instance, Luhar and Nepf (2011) developed a scaling model for the drag of smaller seagrasses in currents by considering the different balances between drag, buoyancy, and rigidity. Luhar and Nepf (2016) and Lei and Nepf (2019) extended this work to wave conditions and the meadow scale, mainly focusing on seagrasses for which hydrodynamic forcing is primarily balanced by blade stiffness. Henderson (2019) complemented this work by also analyzing drag reduction in plants where drag forces are balanced by both stiffness and buoyancy.

Notably, most of the past work has been conducted with the assumption of drag dominated flows; that is, inertial forces such as the pressure gradient and added mass forces are insignificant when compared to drag forces and do not contribute much to plant motion. This is relatively accurate for smaller seagrass species, which usually grow in very shallow waters. However, kelp often grows in deeper waters and fronds can be quite long. Furthermore, typical wave conditions of coastal California create a natural environment where inertial forces become important. Together, all of these factors (longer plant lengths, the importance of inertial forces, the predominance of buoyancy over bending stiffness as a restoring force) produce distinct dynamical behavior and lead to different laws of drag reduction.

Thus, the purpose of this study is to gain a better understanding of kelp hydrodynamics by investigating the impact of inertial forces on kelp motion and consequently, kelp drag reduction. We first develop a generalized numerical model for kelp frond motion, and the model is then used to study the response of kelp fronds to different wave conditions observed on the coast of California. We focus specifically on the importance of inertial forces and how that impacts different aspects of frond motion and drag reduction.

2 Methods

2.1 Model Description

We constructed a two dimensional model for the motion of an individual kelp frond following the approach outlined by Rosman et al. (2013) and Marjoribanks et al. (2014), which can be considered as a refinement of the simple tethered-buoy model developed by Utter and Denny (1996). The kelp frond is discretized into n segments, and each segment is modeled as a point mass attached to a string with the flexibility and tensile stiffness of kelp stipes. Thus, the kelp frond is modeled as a set of point masses connected by strings. The position of each point mass is represented by the vector $\mathbf{x}_i = (x_i, z_i)$, and its velocity by the vector $d\mathbf{x}_i/dt$. A visualization of this representation is given in Fig. 1(b). Note that kelp usually grows to form a dense canopy floating on the surface that can significantly enhance the total drag (Rosman et al., 2013). For simplicity, we do not consider the presence of the surface canopy here, and focus only on situations in which the frond length is smaller than the water depth.

The motion of each point mass is governed by Newton's second law. Following Utter and Denny (1996), Denny et al. (1997), and Rosman et al. (2013), we use Morison's equation (e.g., see Journee & Massie, 2000) to describe the forces acting on kelp. In the present model, we included the five main forces that determine kelp motion: buoyancy, drag, added mass, pressure gradient, and tension. We assume that the drag is exerted by the area of the blades, the bending stiffness originates from the kelp stipe, and the buoyancy comes from the pneumatocysts. Because kelp stipes are very flexible, we assume that their rigidity, or resistance to bending, is negligible. As in Utter and Denny (1996), we also neglect lift and skin friction forces, which are rel-

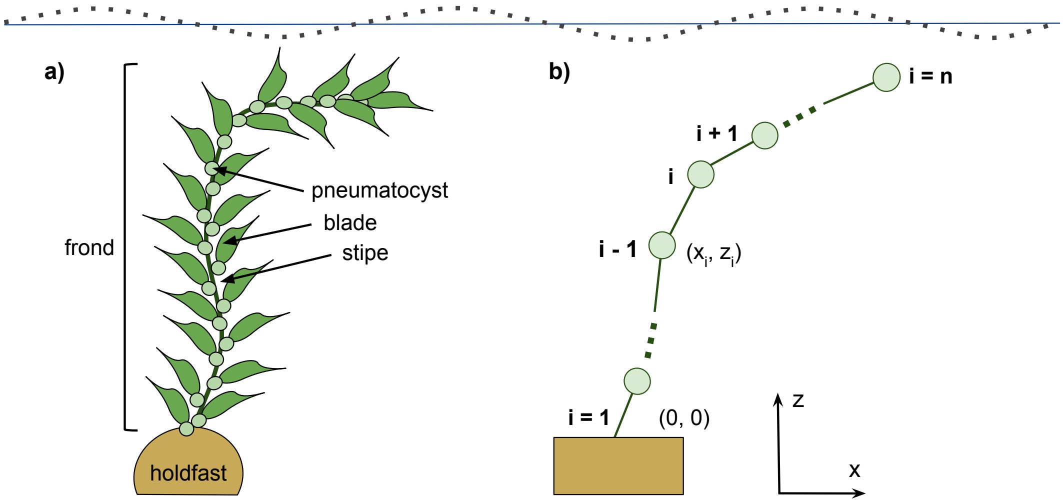

Figure 1. (a) *M. pyrifera* frond and (b) schematic of the discretization of the frond in the numerical model.

atively inconsequential. Assuming each segment has an effective mass m_k, the governing equation of motion for the i^{th} segment is given by

$$m_k \frac{d^2\mathbf{x}_i}{dt} = \mathbf{F}_{D,i} + \mathbf{F}_{B,i} + \mathbf{F}_{P,i} + \mathbf{F}_{AM,i} + \mathbf{F}_{T,i} + \mathbf{F}_{T,i+1}, \tag{1}$$

where $\mathbf{F}_{D,i}$ is the drag force, $\mathbf{F}_{B,i}$ is the buoyant force, $\mathbf{F}_{P,i}$ is the pressure gradient force, $\mathbf{F}_{AM,i}$ is the added mass force, and $\mathbf{F}_{T,i}$ and $\mathbf{F}_{T,i+1}$ are the tension forces on the strings that connect the point mass to its neighboring masses.

The drag force is modeled using a quadratic equation given in terms of relative velocity

$$\mathbf{F}_{D,i} = \frac{1}{2}\rho_w C_d A_i \left|\mathbf{u}_i - \frac{d\mathbf{x}_i}{dt}\right| \left(\mathbf{u}_i - \frac{d\mathbf{x}_i}{dt}\right), \tag{2}$$

where ρ_w is the density of seawater, C_d is the drag coefficient, A_i is the maximal projected area of each frond segment, and $\mathbf{u}_i = (u_{x,i}, u_{z,i})$ is the two-dimensional fluid velocity vector. Contrary to most models of seagrass dynamics (Luhar & Nepf, 2011, 2016), we assume that there is no reduction in exposed area with bending. This is because as kelp fronds bend, their blades remain oriented with the flow, so the exposed area changes very little (e.g., the contribution of the area of the stipe to the drag force is negligible).

The buoyancy force is given by

$$\mathbf{F}_{B,i} = (\rho_k - \rho_w)V_i\mathbf{g}, \tag{3}$$

where ρ_k is the density of the kelp frond, V_i is the volume of each segment, and $\mathbf{g}$ is the gravitational acceleration vector.

Two forces are associated with the acceleration of the fluid: the pressure gradient force (or Froude-Krylov force) and the added mass force. They are given, respectively, by

$$\mathbf{F}_{P,i} = \rho_w V_i \frac{\partial \mathbf{u}_i}{\partial t} \tag{4}$$

and

$$\mathbf{F}_{AM,i} = C_a \rho_w V_i \left(\frac{\partial \mathbf{u}_i}{\partial t} - \frac{d^2 \mathbf{x}_i}{dt} \right), \tag{5}$$

where C_a is the added mass coefficient. We will refer to these two forces as the inertial forces acting on the kelp frond.

In oscillatory flows, it is typical to model the drag and added mass coefficients (C_d and C_a) as a function of the Keulegan-Carpenter number (KC), which characterizes the ratio between inertial and drag forces (e.g., see Luhar & Nepf, 2016). This is done based on experiments with flat plates and similar objects in oscillatory flow (Keulegan & Carpenter, 1956; Sarpkaya & O'Keefe, 1996), for which $KC = U_w T_p / d$, where U_w is a characteristic velocity scale, T_p is the wave period, and d is the thickness of the plate. These effects are attributed to the vortex shedding from these blunt objects and there is little reason to believe that kelp fronds have a similar behavior. Therefore, we do not include explicit effects of KC on C_d and C_a in our model.

Each point mass is also subject to tension forces from the string connected to the point mass below, $\mathbf{F}_{T,i}$, and to the point mass above, $\mathbf{F}_{T,i+1}$. Thus, the total tension force on each segment is given by the sum of the two tensions, or

$$\mathbf{F}_{T,i} + \mathbf{F}_{T,i+1} = -EA_c \frac{|\mathbf{x}_i - \mathbf{x}_{i-1}| - l_i}{l_i} \mathbf{e}_{s,i} + EA_c \frac{|\mathbf{x}_{i+1} - \mathbf{x}_i| - l_{i+1}}{l_{i+1}} \mathbf{e}_{s,i+1}, \tag{6}$$

when $|\mathbf{x}_i - \mathbf{x}_{i-1}| > l_i$ and $|\mathbf{x}_{i+1} - \mathbf{x}_i| > l_{i+1}$, where l_i and l_{i+1} are the lengths of each segment. Here we have adopted the elastic model used by Utter and Denny (1996) to represent the tension on the string, and E is the modulus of elasticity of the kelp, while $\mathbf{e}_{s,i}$ and $\mathbf{e}_{s,i+1}$ are the unit vectors in the direction of their respective segments. We assume that $\mathbf{F}_{T,i} = 0$ at the tip of the frond (last segment, $i = n$), and that the plant is rooted at $\mathbf{x}_0 = (0,0)$. Note that by adopting this model and solving for the tension force explicitly, our model allows for stretching and compression of each frond segment.

The complete equation after dividing all terms by the total volume occupied by each kelp segment is

$$\begin{aligned}(\rho_k + C_a \rho_w) \frac{d^2 \mathbf{x}_i}{dt} = \quad & \tfrac{1}{2} \rho_w C_d \tfrac{A_i}{V_i} \left| \mathbf{u}_i - \tfrac{d\mathbf{x}_i}{dt} \right| \left(\mathbf{u}_i - \tfrac{d\mathbf{x}_i}{dt} \right) + (\rho_k - \rho_w)\mathbf{g} + (\rho_w + C_a \rho_w) \tfrac{\partial \mathbf{u}_i}{\partial t} \\ & + \tfrac{EA_c}{V_i} \left(- \tfrac{|\mathbf{x}_i - \mathbf{x}_{i-1}| - l_i}{l_i} \mathbf{e}_{s,i} + \tfrac{|\mathbf{x}_{i+1} - \mathbf{x}_i| - l_{i+1}}{l_{i+1}} \mathbf{e}_{s,i+1} \right) \end{aligned} \tag{7}$$

where the effective mass m_k is given by $V_i(\rho_k + C_a\rho_w)$. The set of equations (7) is numerically integrated in time using a fourth-order Runge-Kutta algorithm to solve for the position of all point masses $\mathbf{x}_i = (x_i, z_i)$ and associated velocities. In our current model implementation, all the segment have the same geometrical properties such that A_i, l_i, and V_i are all constant for all i.

The main differences between our modeling approach and the more standard models used for seagrass (e.g., Marjoribanks et al., 2014; Zeller et al., 2014; Luhar & Nepf, 2016) are that: (1) we neglect bending stiffness given that the restoring force to resist motion in kelp is mostly provided by the buoyancy force, and models that include bending stiffness for low stiffness systems generate numerical instability issues such as poor convergence (Zeller et al., 2014); (2) we allow for elastic stretching deformation instead of imposing a constant frond length, which is important in modeling kelp motion (Johnson & Koehl, 1994; Utter & Denny, 1996). As an aside, we attempted to use the model developed by (Luhar & Nepf, 2016) to simulate some of our cases, but ran into numerical instability issues even for the shortest fronds under the least energetic wave conditions despite using a very fine grid resolution and small time step.

2.2 Model Setup

We study frond motion by imposing a two-dimensional linear wave flow field represented by $\mathbf{u} = (u_x, u_z)$. For a coordinate system located at the bottom of the ocean, the wave orbital velocity components at a location (x, z) are given by (Dean & Dalrymple, 1991):

$$\begin{cases} u_x = A_w\omega\dfrac{\cosh(kz)}{\sinh(kH)}\cos(kx - \omega t) \\ u_z = A_w\omega\dfrac{\sinh(kz)}{\sinh(kH)}\sin(kx - \omega t) \end{cases} \tag{8}$$

where A_w is the wave amplitude, ω is the wave frequency, k is the wavenumber, and $H = 12$ m is the depth of the water column (note that in this coordinate system, $z = H$ at the surface).

To investigate the motion of kelp in its natural habitat, we utilized buoy data from the Coastal Data Information Program (CDIP; `https://cdip.ucsd.edu`). More specifically, buoys 87, 88, and 89 recorded local wave conditions in real kelp forests along the coast of the Channel Islands (Santa Rosa and Santa Cruz Islands) from October 1995 through December 1995. We used their measurements of significant wave height, H_s, and peak wave period, T_p, to determine typical wave conditions within natural kelp forests on the California coast. The joint probability density function of measured significant wave height and wave period is shown in Fig. 2. In total, we selected sixteen different wave conditions covering the full realistic range of observed waves. For the simple monochromatic wave model, we approximated the wave amplitude as $A_w = H_s/2$ and cal-

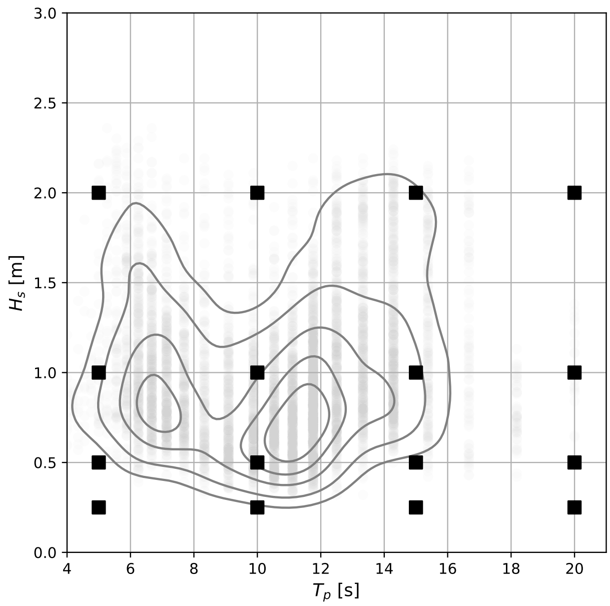

Figure 2. Simulated wave conditions. Light gray circles represent the aggregated CDIP measurements, and the gray lines represent the probability density function of the data (levels: 0.1, 0.25, 0.5, 0.75, 0.9). Black squares represent the conditions we selected for our runs. Data from CDIP, Scripps Institution of Oceanography.

culated the wave frequency from $\omega = 2\pi/T_p$ and the wave number from the dispersion relation $\omega = \sqrt{gk\tanh(kH)}$. The resulting waves fall in the range of $1/3 < kH < 2$, so we avoid using approximations for deep-water or shallow-water waves.

The kelp properties used in the model were mostly compiled from Utter and Denny (1996), and these values are presented in Table 1. Here, the kelp density ρ_k is supposed to represent the bulk density of the frond, including the gas-filled pneumatocysts. The value adopted here was obtained from Rosman et al. (2013) and was confirmed from measurements of frond mass and volume (K. A. Davis unpubl.). Notably, this is about 40% larger than the value adopted by Henderson (2019). The drag coefficient adopted here is from the intercept of the drag-velocity plot by Utter and Denny (1996) (i.e., the drag for a rigid frond), and it is in good agreement with the mode of the distribution obtained by Monismith et al. (2022) for intermediate biomass kelp forests. Finally, we obtained an estimate of frond volume indirectly from the frond projected area, the average mass per unit area, and the frond density.

Table 1. List of kelp properties and their associated variables and values. All values are from (Utter & Denny, 1996), except for ρ_k which is taken from (Rosman et al., 2013).

Variable	Description	Value
ρ_k	Density of kelp	850 [kg m^{-3}]
ρ_w	Density of seawater	1025 [kg m^{-3}]
C_a	Added mass coefficient	3
C_d	Drag coefficient	0.0148
l	Frond length	2, 5, 10 [m]
A	Maximal projected area of a frond	$0.297 \times l^{0.955}$ [m^2]
A_c	Cross-sectional area of a stipe	4.1×10^{-5} [m^2]
M_A	Average mass per unit area	0.774 [kg m^2]
V	Estimated volume of frond	$V = \frac{M_A A}{\rho_k}$ [m^3]
E	Modulus of elasticity	1.91×10^7 [Pa]

For each of the sixteen wave parameters, we tested three different frond lengths: 2 m, 5 m, and 10 m. Because kelp fronds can grow to be quite large, these lengths were selected in order to illustrate how kelp behaves in different wave conditions over its entire life cycle. This combination of plant length and wave conditions resulted in 48 simulations (see Table 2). Out of these cases, there were two that showed unrealistic amounts of stretching and compression (i.e. larger than 1% of the frond length) due to the elasticity of the kelp stipe: (1) $l = 10$ m, $H_s = 1$ m, $T_p = 5$ s; (2) $l = 10$ m, $H_s = 2$ m, $T_p = 5$ s. Thus, we removed these two cases from further analysis. The wave conditions in the removed cases are exceptionally high energy, and rarely occur in the real world (see Fig. 2). We postulate that realistically, kelp fronds would probably become dislodged in those extreme, storm like wave conditions.

Each model kelp frond is discretized into 50 nodes, and initially starts at rest in a vertically upright position. To maximize accuracy while preserving stability, we set a time step of $\Delta t = T_p/10000$. We found that generally, the model kelp fronds required 5-7 wave periods before reaching an equilibrium cycle. Thus, we ran each simulation for 10 wave cycles, and only data from the last wave cycle were utilized for analysis. Tests showed no sensitivity of the results to using more nodes or reducing the time step.

It is rather difficult to perform validation of our code, as most detailed data from flume experiments available (e.g. Zeller et al., 2014; Luhar & Nepf, 2016) is for systems in which the bending stiffness is important. Therefore, we validate the model and test the assumption that stiffness is not important against the theory for steady flow developed by Luhar and Nepf (2011), and present results for the range of kelp and wave properties relevant to our study in Appendix A.

2.3 Theory

Luhar and Nepf (2016) first introduced three dimensionless parameters that govern blade motion in wave conditions: the Cauchy number (Ca), buoyancy parameter (B), and the ratio of blade length to wave excursion (L). These parameters are given by

$$Ca = \frac{\frac{1}{2}\rho_w C_d A U_w^2}{\frac{EI}{l^2}} \tag{9}$$

$$B = \frac{(\rho_w - \rho_k) g V}{\frac{EI}{l^2}} \tag{10}$$

$$L = \frac{l\omega}{U_w} = \frac{l}{\Delta x_w} \tag{11}$$

Note that quantities denoted without the subscript i refer to the same variable for the entire frond instead of per segment (e.g., A_i is the projected frond area for each segment in the numerical model, while A is the projected area for the entire frond).

The Cauchy number Ca represents the ratio of drag forces (the most common force driving plant motion) to restoring force due to stiffness, while B represents the ratio of buoyancy to stiffness (i.e., the two forces that act to reduce plant motion). The parameter L also impacts blade dynamics, as is discussed below. Here, I is the second moment of area (for kelp stipes with circular cross-sectional area, $I = \pi r_s^4/4$, where r_s is the radius of the stipe), and U_w and Δx_w are characteristic scales for the horizontal wave orbital velocities and excursions, respectively. Because kelp fronds are typically much longer and grow in deeper water than seagrasses, the variation of the wave orbital velocity along the length of the frond can be important. We define U_w as the amplitude of the horizontal wave orbital velocity averaged over the length of the frond

$$U_w = \frac{1}{l}\int_0^l A_w \omega \frac{\cosh(kz)}{\sinh(kH)} dz = \frac{A_w \omega}{kl} \frac{\sinh(kl)}{\sinh(kH)}. \tag{12}$$

Consequently, we also define Δx_w as an average along the length, or $\Delta x_w = U_w/\omega$. In this way, L is interpreted as the ratio between frond length and average horizontal wave excursion. Note that as a result of our definition of U_w, any parameter that is function of U_w implicitly takes into account the impact of wave decay with depth.

In most seagrasses, drag is the main force driving motion, bending stiffness is the main restoring mechanism, buoyancy in negligible, and blade dynamics and drag reduction can be fully characterized by Ca and L. In steady flow, for $Ca \ll 1$, the blade remains upright and has very little drag reduction (Luhar & Nepf, 2011). For $Ca \gg 1$, significant bending occurs before the restoring force balances the drag force and this reconfiguration allows for a large drag reduction (via reduction in the plant surface area). In unsteady flows, drag reduction in the $Ca \gg 1$ limit also depends on the excursion of the blade, which Luhar and Nepf (2016) quantified using L. When $L \ll 1$, the blade length is much smaller than the wave excursion, so the blade should reach a maximum excursion while the fluid continues traveling past it. Thus, the blade behaves similarly as in steady flows, and drag reduction in this limit is still only dependent on Ca. On the other hand, when $L \gg 1$, the blade length is much larger than the wave excursion, so we expect that only the tip moves with the wave orbital velocity. The majority of the plant is akin to a rigid blade, and drag reduction is proportional to the product CaL.

Unlike seagrasses, kelp rigidity is very low (the stipe is very flexible), while buoyancy is very high. Therefore, drag forces are primarily balanced by buoyancy. As a result, for most wave conditions, stiffness plays an insignificant role in kelp motion (i.e, $Ca \gg 1$ and $B \gg 1$). Thus, for our cases, the buoyancy parameter

$$P = \frac{\frac{1}{2}\rho_w C_d A U_w^2}{(\rho_w - \rho_k) g V} = \frac{Ca}{B}, \tag{13}$$

first introduced by Nikora et al. (1998) is more relevant. Note that P is equivalent to Ca, except it measures the magnitude of the drag force in comparison to the resistance to bending provided by buoyancy. This definition is consistent with Henderson (2019), which built on previous results to develop a framework for the analysis of the response of aquatic vegetation to wave forcing in the presence of both buoyancy and stiffness. In particular, they identified the joint importance of CaL and PL in governing plant motion and drag reduction.

All of the studies discussed above start from the assumption that the Keulegan-Carpenter number is large and that the drag force is the main driver of blade motion. As we will show later, in many of our simulations, inertial forces are larger than the drag forces. To characterize this effect, we define the Keulegan-Carpenter number as

$$KC = \frac{\frac{1}{2}\rho_w C_d U_w^2}{\rho_w d(1 + C_a) U_w \omega} = \frac{C_d}{2(1 + C_a)} \frac{U_w}{\omega d}, \tag{14}$$

where d is a thickness associated with the cross sectional area ($d = V/A$). This specific definition, instead of the more traditional $KC = 2\pi U_w/(\omega d)$, is motivated by the scale analysis of the equations of frond motion and will be further discussed in Sec. 2.3.1.

For the wave and kelp conditions studied here, the values of B lie in the range of $O(10^3) < B < O(10^6)$, indicating that buoyancy forces are the dominant restoring forces preventing mo-

Table 2. List of numerical simulations and their associated dimensionless parameters defined in Equations (13), (11), and (14). Wave periods of 5 s, 10 s, 15 s, 20 s correspond with wave numbers of 0.167 m^{-1}, 0.063 m^{-1}, 0.04 m^{-1}, 0.03 m^{-1}, respectively.

H_s [m]	T_p [s]	$l = 2$ [m]			$l = 5$ [m]			$l = 10$ [m]		
		P	L	KC	P	L	KC	P	L	KC
0.25	5	0.0094	57.2	0.071	0.011	130.0	0.078	0.021	189.9	0.11
0.25	10	0.044	13.3	0.31	0.045	32.7	0.31	0.050	62.2	0.33
0.25	15	0.054	8.0	0.51	0.054	19.8	0.51	0.056	38.8	0.52
0.25	20	0.055	5.9	0.69	0.056	14.7	0.69	0.057	29.0	0.70
0.5	5	0.038	28.6	0.14	0.045	65.0	0.16	0.085	95.0	0.21
0.5	10	0.18	6.6	0.61	0.18	16.3	0.62	0.20	31.1	0.65
0.5	15	0.22	4.0	1.02	0.22	9.9	1.03	0.23	19.4	1.05
0.5	20	0.22	2.9	1.38	0.22	7.3	1.40	0.23	14.5	1.40
1	5	0.15	14.3	0.28	0.18	32.5	0.31	0.34	47.5	0.43
1	10	0.70	3.3	1.23	0.72	8.2	1.24	0.79	15.6	1.31
1	15	0.86	2.0	2.04	0.87	5.0	2.05	0.90	9.7	2.09
1	20	0.89	1.5	2.76	0.89	3.7	2.77	0.91	7.2	2.80
2	5	0.60	7.2	0.57	0.73	16.3	0.63	1.36	23.7	0.86
2	10	2.80	1.7	2.45	2.88	4.1	2.49	3.17	7.8	2.61
2	15	3.43	1.0	4.08	3.47	2.5	4.1	3.61	4.9	4.18
2	20	3.55	0.74	5.53	3.57	1.8	5.54	3.65	3.6	5.61

tion and that bending stiffness can be safely neglected (see also discussion in the appendix). The corresponding values of the Cauchy number are $O(10) < Ca < O(10^6)$. Thus, the relevant parameters characterizing our simulations are P, L, and KC, and values are listed on Table 2.

2.3.1 Scaling

To gain some insight into frond behavior, we follow the approach used by Henderson (2019) and start from a horizontal force balance of the governing equation of frond motion, Eq. (7). Here, we write the equation for the entire kelp frond, as opposed to the discrete version we use in the numerical model. In particular, Henderson (2019) assumes an equilibrium (i.e., a force balance with no frond acceleration) and neglects the vertical velocities. Instead, we keep the horizontal acceleration term and write Eq. (7) as

$$\begin{cases} (\rho_k + C_a\rho_w)\dfrac{du_k}{dt} = \dfrac{1}{2}\rho_w C_d \dfrac{A}{V}|u_x - u_k|(u_x - u_k) + (\rho_w + C_a\rho_w)\dfrac{\partial u_x}{\partial t} + \dfrac{EA_c}{V}\left(\dfrac{|\mathbf{x}| - l}{l}\right)\sin\theta \\ -(\rho_k - \rho_w)g + \dfrac{EA_c}{V}\left(\dfrac{|\mathbf{x}| - l}{l}\right)\cos\theta = 0 \end{cases} \tag{15}$$

Here, θ is the angle of deflection from the vertical, u_x is the representative horizontal wave velocity at the frond tip, u_k is the horizontal component of the tip velocity of the kelp $d\mathbf{x}/dt$, and $\mathbf{x}$ is the position of the frond tip. We proceed by assuming that θ is small enough so that the small angle approximation $\cos\theta \approx 1$ can be invoked, reducing the vertical balance in (15) to

$$(\rho_k - \rho_w)g = \frac{EA_c}{V}\left(\frac{|\mathbf{x}| - l}{l}\right) \tag{16}$$

which yields the new horizontal balance

$$(\rho_k + C_a\rho_w)\frac{du_k}{dt} = \frac{1}{2}\rho_w C_d d|u_x - u_k|(u_x - u_k) + (\rho_w + C_a\rho_w)\frac{\partial u_x}{\partial t} + (\rho_k - \rho_w)g\frac{x}{l} \tag{17}$$

Note that we also used $\sin\theta = x/l$.

Normalizing by ρ_w, U_w, ω, and Δx_w, Eq. (17) can be written as

$$\frac{PL}{KC}\left[\frac{du_k^*}{dt^*} - \frac{\partial u_x^*}{\partial t^*}\right] = PL\left[|u_x^* - u_k^*|(u_x^* - u_k^*)\right] + [x^*]\,, \tag{18}$$

where we used the approximation $\frac{(\rho_k/\rho_w + C_a)}{(1+C_a)} \approx 1$. Here, all the terms denoted by * are dimensionless and assumed to be of order unity.

The equivalent equation for the force balance (i.e., assuming no acceleration) as done in Henderson (2019) is given by

$$\frac{PL}{KC}\left[-\frac{\partial u_x^*}{\partial t^*}\right] = PL\left[|u_x^* - u_k^*|(u_x^* - u_k^*)\right] + [x^*]\,. \tag{19}$$

The more complete Eq. (18) and its force balance version (19) both suggest the use of PL and PL/KC as two main scaling parameters. A visualization of this two-dimensional parameter space is given in Fig. 3.

It is useful to understand the behavior of kelp fronds in three asymptotic regimes: (1) the "buoyancy dominated" regime, given by $PL \ll 1$ and $PL/KC \ll 1$ and corresponding to points in the red region and closer to the origin in Fig. 3(a), (2) the "drag dominated" regime, given by $PL \gg 1$ and $KC \gg 1$ and corresponding to points in the blue region and closer to the bottom right corner of Fig. 3(a), and (3) the "inertia dominated" regime, given by $PL/KC \gg 1$ and $KC \ll 1$ and corresponding to points in the yellow region and closer to the top left corner of Fig. 3(a).

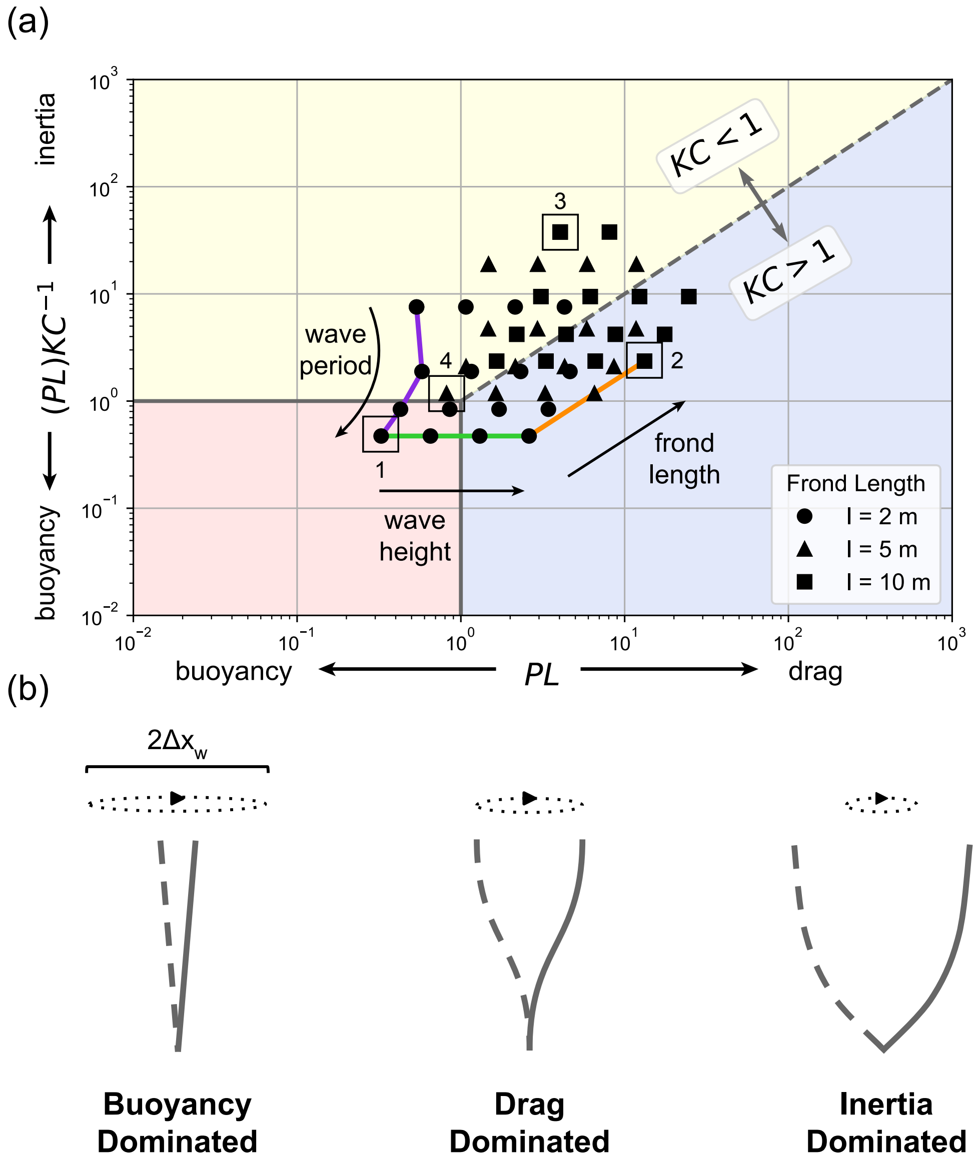

Figure 3. (a) The parameter space for kelp motion. The red region represents where motion is buoyancy dominated; blue represents where motion is drag dominated; yellow represents where motion is inertia dominated. The gray lines represent the dividers $PL = 1$, $PL/KC = 1$, and the dashed gray line is $KC = 1$. The black points are where our simulations fall, where different shapes represent each of the plant lengths. The purple, green, and orange solid lines show increasing wave period, wave height, and plant length, respectively. Black squares 1, 2, 3, and 4 denote cases selected for further analysis in later sections. (b) Expected kelp motion in each asymptotic regime.

In the "buoyancy dominated" regime, Eq. (18) suggests $x^* \ll 1$, which implies $x \ll \Delta x_w$ (i.e., Δx_w is not the appropriate scale for the horizontal excursion of the tip). Here, buoyancy is very strong and severely limits plant motion as depicted in Fig. 3(b). This is equivalent to the nearly rigid plant configuration considered by both Luhar and Nepf (2016) and Henderson (2019).

The "drag dominated" regime corresponds to the small excursion limit of Luhar and Nepf (2016) and Henderson (2019). Here, drag forces are much larger than inertial forces and the frond motion is driven mostly by drag. In this case, the left hand side of Eq. (18) is approximately 0, resulting in the following simplification:

$$|u_x^* - u_k^*|(u_x^* - u_k^*) = \frac{|x^*|}{PL}. \tag{20}$$

Since $PL \gg 1$, it is expected that cases in this regime should have small relative velocity, or that $|u_x^* - u_k^*|(u_x^* - u_k^*) \ll 1$. The frond should move closely with the wave motion, meaning that $x^* \approx 1$, or $x \approx \Delta x_w$ as illustrated in Fig. 3(b).

Finally, in the "inertia limit", inertial forces are much larger than drag and buoyancy. Thus, we can assume that

$$\frac{PL}{KC}\left[\frac{du_k^*}{dt^*} - \frac{\partial u^*}{\partial t^*}\right] \gg PL\left[|u_x^* - u_k^*|(u_x^* - u_k^*)\right], \tag{21}$$

and applying that simplification to Eq. (18) yields

$$\frac{PL}{KC}\left[\frac{du_k^*}{dt^*} - \frac{\partial u^*}{\partial t^*}\right] = [x^*]\,. \tag{22}$$

Because $PL/KC \gg 1$, this requires

$$\left[\frac{du_k^*}{dt^*} - \frac{\partial u_x^*}{\partial t^*}\right] \propto \left(\frac{PL}{KC}\right)^{-1}, \tag{23}$$

implying that the two accelerations are of the same order of magnitude. In practice, this means that the frond acceleration is mostly caused by the same pressure gradient force that is driving the wave motion. Because kelp is less dense than the fluid ($\rho_k < \rho_w$), the frond acceleration in response to the same pressure gradient force is larger than that of a fluid parcel, causing the frond to perform an orbital motion with larger horizontal displacements than the fluid itself. Hence, when $PL/KC \gg 1$, we also have $x^* = x/\Delta x_w > 1$, meaning that it is possible for the kelp excursion to be greater than the wave excursion.

2.3.2 Drag Coefficient Scaling

The varying flexibility of aquatic vegetation can reduce the drag force exerted on the flow by two mechanisms: (1) a reduction of the frontal area exposed to the flow, and (2) a reduction in the relative velocity due to synchronous motion of vegetation and water. Luhar and Nepf (2011) quantified this effect by defining the effective length, l_e, which represents the length of a rigid blade that generates the same drag as a flexible blade of length l. Physically, l_e/l represents the ratio of the real horizontal drag force (F_D) to the horizontal drag force experienced by a rigid blade ($F_{D,Rig}$). Alternatively, it is equivalent and sometimes more convenient to define a reduced drag coefficient $C_{d,f}$ to represent the effect of motion on the drag force (Razmi et al., 2020), or

$$\frac{l_e}{l} = \frac{F_D}{F_{D,Rig}} = \frac{C_{d,f}}{C_d}. \tag{24}$$

If $C_{d,f}$ is known, one can calculate the true drag force using the fluid velocity (without explicit knowledge of the vegetation motion) via

$$F_D = \frac{1}{2}\rho_w C_{d,f} A|u_x|u_x. \tag{25}$$

The drag reduction due to plant motion is modeled by the reduced value of $C_{d,f}$ (when compared to C_d).

Luhar and Nepf (2016) found that for plants where the restoring force is primarily from the bending rigidity, $C_{d,f}/C_d \propto (CaL)^{-1}$. Henderson (2019) considered the case with both bending rigidity and buoyancy when the motion is driven by a linearized drag force. Their solution recovers the result from Luhar and Nepf (2016) when buoyancy in negligible and yields a new result for the case of interest here, where buoyancy is the dominant restoring mechanism. In this case, their result yields

$$\frac{C_{d,f}}{C_d} = \left[\frac{\pi^2/(4PL)^2}{1+\pi^2/(4PL)^2}\right]^{1/4}, \tag{26}$$

which transitions from a region in which $C_{d,f}/C_d \approx 1$ in the buoyancy dominated regime to $C_{d,f}/C_d \propto (PL)^{-1/2}$ for large PL in the drag dominated regime. Previous studies did not consider the cases where inertia is important ($KC \ll 1$), and it is unclear how that would impact the total drag force.

2.3.3 Parameter Space

The cases shown in Table 2 are presented on the parameter space formed by PL and PL/KC in Fig. 3. For most wave conditions, our simulations are in a transition region ($KC \approx 1$, $PL \approx 1$, or $PL/KC \approx 1$), so we do not expect to observe results that resemble the asymptotic conditions discussed in Section 2.3.1. Note that most studies to date have focused on the regime in which $KC \gg 1$, investigating motion and drag in the transition between the red and blue regions.

To facilitate interpretation of our results presented in the next sections, we have included in Fig. 3 arrows indicating how varying wave properties and frond length impact the location of points on the parameter space. Wave orbital velocity amplitudes are proportionate to $A_w\omega$, so larger wave periods (and smaller wavenumbers) generally leads to smaller PL and larger KC values. In other words, increasing wave period (reducing wavelength) results in cases where buoyancy is relatively larger and drag is more important than inertial forces. Lines of increasing wave height have constant PL/KC values (parallel to the x-axis in Fig. 3), transitioning further away from the limiting behavior of buoyancy or inertia dominated regimes into the drag dominated regime. Similarly, only increasing frond length does not affect KC, but correlates with increasing PL and PL/KC values, meaning buoyancy becomes relatively less important.

3 Results and Discussion

3.1 Characterization of Kelp Motion

In general, model kelp responded to different wave conditions with a wide range of behavior. Initially, all upright fronds undergo an adjustment period that lasts a few wave periods before they reach an equilibrium cycle, the type of which depends on where the simulation falls in the parameter space of Fig. 3(a).

Fig. 4 shows example frond excursion plots for different regimes of kelp motion: buoyancy dominated, drag dominated, inertia dominated, and a transition case (refer back to Figure 3(a) for where each case is located in the parameter space). Animations for these four cases are presented in the Supporting Information. For each case, we also show how the relative horizontal frond excursion

$$\delta x = \frac{(x_{\max} - x_{\min})}{2\delta x_w(\bar{z})} \tag{27}$$

varies along the length of the plant. Here, $2\delta x_w(\bar{z})$ is the local horizontal wave excursion at the mean vertical position of each segment over the wave cycle, or

$$\delta x_w(\bar{z}) = A_w\omega \cosh(k\bar{z})/\sinh(kH) \tag{28}$$

Physically, δx is a measure of the frond excursion normalized by the average wave excursion.

In the buoyancy dominated region of the parameter space (Case 1, Fig. 4a), the frond excursion is less than the wave excursion as the entire frond remains mostly upright. The maximum frond excursion is <90% of the horizontal wave excursion. In this case, $PL \approx 0.3$ and $(PL)/KC \approx 0.5$, so buoyancy is only around 2-3 times larger than the other forces, which is why the blade ex-

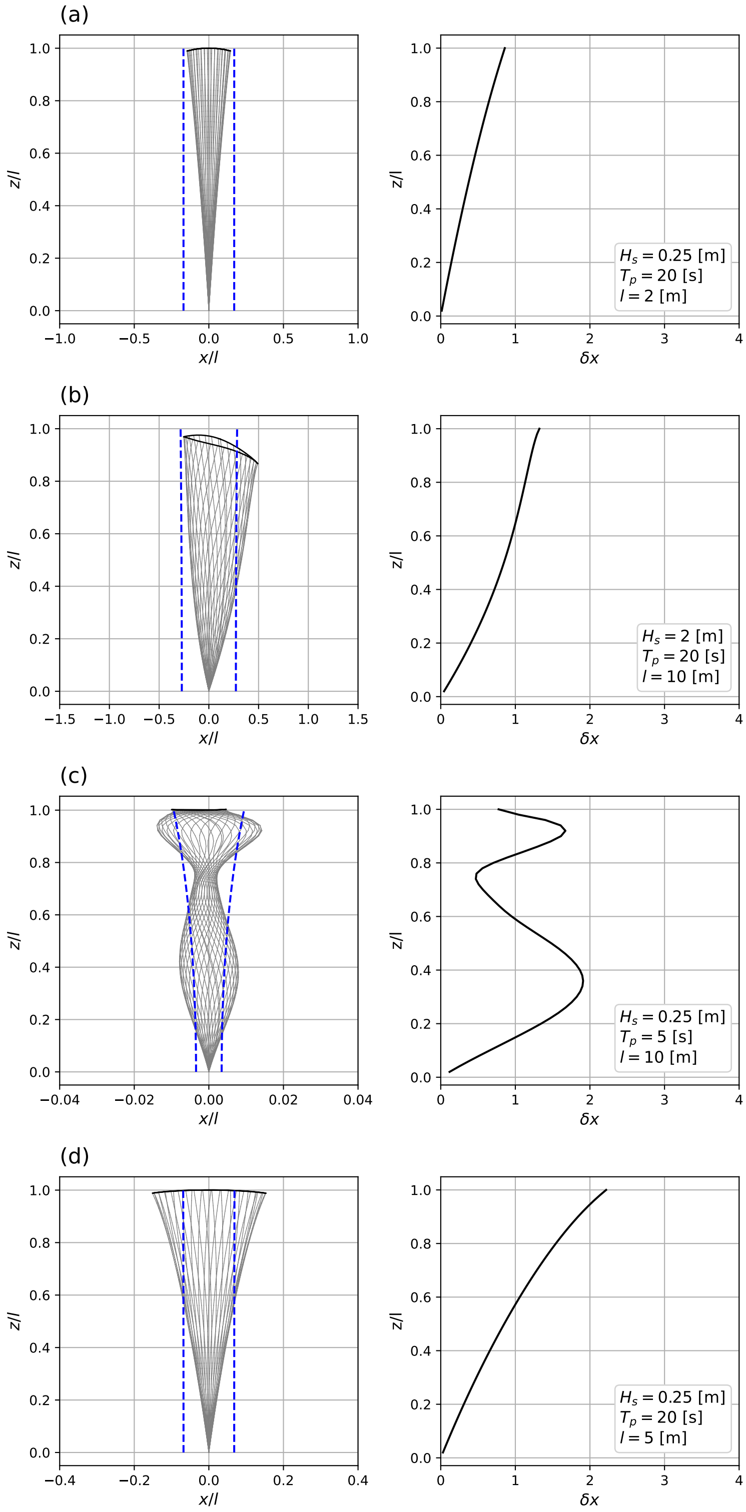

Figure 4. The cases of kelp motion from different regions of the parameter space; see Figure 3(a). Left panels are blade excursions over one equilibrium wave cycle; blue dashed lines represent the horizontal wave excursion at each depth. Both axes are normalized by plant length (l). Right panels are relative horizontal excursion plots for the buoyancy dominated case. (a) Case 1: buoyancy dominated. (b) Case 2: drag dominated. (c) Case 3: inertia dominated. (d) Case 4: transition.

cursion is still fairly large. As points move farther into the buoyancy dominated regime (closer to the origin in the parameter space), we expect that the maximum blade excursion would decrease to nearly zero.

For drag dominated cases (Case 2, Fig. 4b), the upper half of the frond moves more-or-less with the wave, while the bottom portion of the frond moves less than the wave excursion around it. A slight concavity in the profile of δx indicates that the majority of drag is being generated in the bottom 50% of the frond, as postulated by Henderson (2019). There is a part of the tip that moves about 30% more than the wave, which we hypothesize may be the additional effects of the inertial forces or asymmetric motion. Overall, this is the classic example of drag reduction in flexible vegetation due to synchronous oscillation with the wave motion (i.e., reduction in relative velocity between the frond and the water).

In the inertia dominated limit (Case 3, Fig. 4c), a majority of the frond (around 60%) moves more than the wave excursion. Note that the displacements are only a small fraction of the plant length, and that the aspect ratio of the figure is highly distorted. The maximum frond excursion is almost twice as large as the wave excursion; this is clearly a much greater effect than in the previous two cases. Different portions of the frond are out of phase with each other (the animation included in Supporting Information is particularly illuminating here), corresponding to a higher natural mode of vibration. This would be equivalent to mode 2 motion identified by Mullarney and Henderson (2010). This higher mode leads to a non-monotonic variation of the amplitude of the frond motion along its length, and we hypothesize that higher inertial forces potentially lead to the amplification of higher natural modes of motion.

Finally, we included a typical example of our transition cases (Case 4, Fig. 4d). Here, the frond excursion plots displays a mix of traits from the other three limits. About half of the frond moves more than the wave, with the tip moving over twice as much as the fluid does. The frond also stays relatively upright and straight, as in the buoyancy dominated regime. Unlike the inertia dominated example, there is a smooth transition in the amplitude of kelp motion.

Despite the large variation in frond motion depending on the dominant forcing mechanisms, some general conclusions are possible. For a fixed frond length l, the relative horizontal blade excursion δx decreases with increasing KC. When $KC < 1$ (inertial forces are larger than drag forces), the entire frond moves more than the wave excursion. On the other hand, when $KC > 1$, a majority of the frond moves less than the wave, with the tip moving about the same. Figure 5 illustrates how the average of δx over the frond length, denoted $\overline{\delta x}$, varies with KC. Clearly,

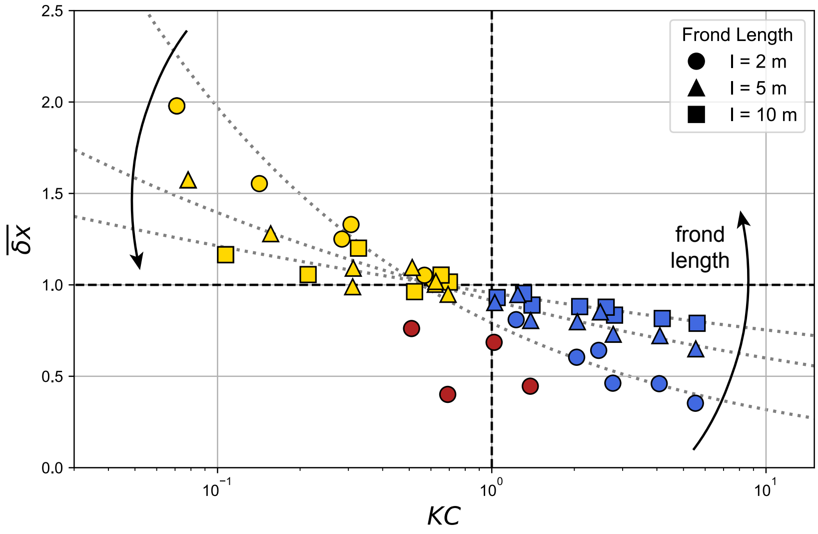

Figure 5. Variation in relative horizontal excursion, averaged over length of the blade ($\overline{\delta x}$) with KC. Yellow points are inertia dominated ($PL/KC > 1$ and $KC < 1$), red are buoyancy dominated ($PL < 1$ and $PL/KC < 1$), and blue are drag dominated ($PL > 1$ and $KC > 1$). Different shapes represent different frond lengths, with circles representing 2 m fronds, triangles are 5 m, and squares are 10 m. Dashed lines were added to facilitate interpretation.

for each frond length, $\overline{\delta x}$ reduces with increasing KC. The buoyancy dominated cases (red symbols) appear as outliers, having much smaller excursions than suggested by the behavior of neighboring points.

Luhar and Nepf (2016) described the relative blade excursion for seagrasses (bending resistance being the dominant restoring force) in the large KC (drag dominated) regime. In particular, they argued that $\overline{\delta x} \approx 1$ for $L \gg 1$ and $\overline{\delta x} \ll 1$ for $L \ll 1$. Note that in our cases, Eqs. (11) and (14) imply $L \propto (l/d)KC^{-1}$. Since we keep the stipe diameter d constant in all our simulations, at a constant value of KC we have $L \propto l$. Results in Fig. 5 agree with Luhar and Nepf (2016) for the large KC regime ($KC > 1$, represented by blue symbols), in that at a fixed value of KC, $\overline{\delta x}$ increases with increasing L and approaches $\overline{\delta x} \approx 1$ for large L. Interestingly, all the frond lengths seem to match the wave excursion for $KC \approx 0.7$, and the behavior switches for values of KC below this threshold (i.e., in the inertia dominated regime) where fronds have larger excursions than the water and $\overline{\delta x}$ increases with decreasing L. In this small KC regime, $\overline{\delta x} \approx 1$ still holds for large L, but $\overline{\delta x} \gg 1$ for $L \ll 1$. Therefore, the unifying conclusion from Fig. 5 valid across the entire KC regime is that $\overline{\delta x} \approx 1$ for $L \gg 1$, and deviations increase with increasing L in different directions depending on the dominant forcing mechanism (drag vs. inertia).

3.2 Characterization of Drag Forces

In our numerical simulations, the drag force is a function of position along the frond and time. We follow Luhar and Nepf (2016) and integrate the horizontal drag force over the frond length, and take its root mean square (RMS) value over one wave cycle to characterize the total drag for each simulation. We verified that as tested by Luhar and Nepf (2016), using the maximum value over the cycle here as well does not produce significant changes. Therefore, we calculate the drag reduction as

$$\frac{C_{d,f}}{C_d} = \frac{[F_D]_{RMS}}{\left[F_{D,Rig}\right]_{RMS}} = \frac{\left[\int_0^l \frac{1}{2}\rho_w C_d a|\mathbf{u} - \frac{d\mathbf{x}}{dt}|(u_x - \frac{dx}{dt})dl\right]_{RMS}}{\left[\int_0^l \frac{1}{2}\rho_w C_d a|\mathbf{u}|u_x dz\right]_{RMS}}, \tag{29}$$

where $a = A/l$ is the maximal frond projected area per unit length (i.e., the frond area density).

Resulting values of $C_{d,f}/C_d$ are displayed as a function of PL and separated by drag dominated ($KC \leq 1$) and inertia dominated ($KC > 1$) regimes in Fig. 6a. As expected, there is good agreement between our drag-dominated cases ($KC > 1$, circles) and the prediction from Henderson (2019) given by Eq. 26. Our own power-law fit to these cases yields

$$C_{d,f}/C_d = (PL)^{-0.6} \tag{30}$$

across the entire range of PL, extending to values larger than 1 for $PL < 1$ (to be discussed below). The small difference in exponent likely originates, among other things, from the linearized drag approximation employed in the derivation of (26) and the presence of inertial forces in our simulations.

On the other hand, the inertia dominated cases ($KC < 1$, triangles) do not scale as well with Eq. (26). Generally, values of $C_{d,f}/C_d$ seem to be independent of KC in the range $PL < 1$, but the power-law decay in the large PL region is steeper for the inertia dominated cases. We expect the drag reduction to be a joint function of PL and KC, but unfortunately our simulated cases are not enough to support a two-dimensional fit with any confidence. Instead, we note that both Eq. (26) and the empirical fit (30) can serve as an upper bound on the true drag. Our best fit for the inertia dominated cases yields $C_{d,f}/C_d = 0.7(PL)^{-0.8}$.

Two important features of Fig. 6 require further explanation: the larger drag reduction in the inertia dominated cases and the increase in drag compared to a rigid frond (i.e. drag augmen-

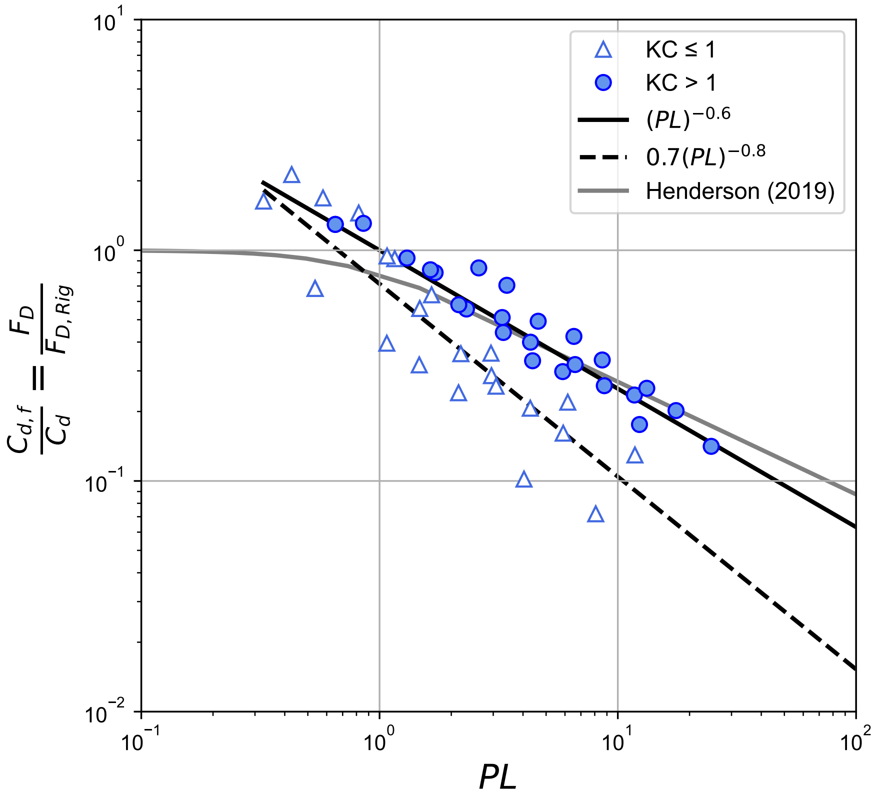

Figure 6. Effective drag coefficients calculated using horizontal drag force only versus PL. The solid black line is the best fit ($R^2 = 0.92$) for cases where $KC > 1$, while the dashed black line is the best fit ($R^2 = 0.86$) for $KC < 1$. The gray line represents Eq. (26). Triangles represent cases where $KC < 1$, while circles are cases where $KC > 1$.

tation) for most cases in which $PL < 1$. To address these questions, we note once again that in our model all changes to drag are caused by the relative velocity between the frond and the water. We define a normalized relative velocity

$$u_{rel} = \frac{(u_x - dx/dt)}{U_w}, \tag{31}$$

and show the variation of u_{rel} over one equilibrium wave period at several locations along the frond in Fig. 7 for the four sample cases illustrated in Fig. 4 (refer to Fig. 8b for the specific $C_{d,f}/C_d$ value corresponding to the cases shown in Fig. 7).

In a typical drag dominated case, the upper portion of the frond moves with the waves, reducing the relative velocities towards the frond tip (e.g., see Figure S1 of the Supporting Information). In this case, most of the drag originates from the bottom of the frond where the relative velocities are comparable to the wave velocity due to restricted frond motion (Luhar & Nepf, 2016; Henderson, 2019). In our selected drag dominated case (Fig. 7b), the behavior is already more complex than that. The relative velocity at a given time switches sign between the bottom and the top of the frond (e.g., at $t/T_p = 0.5$ we have $u_{rel} > 0$ at $z/l = 0.2$ and $u_{rel} < 0$ at $z/l = 1.0$). This change in sign occurs when the frond velocity in the upper portion of the frond is larger than the wave velocity, which happens when the frond excursion is larger than that of the fluid as described in the previous subsection (see Fig. 4b). The cancellation between drag forces from the top and bottom of the frond lead to additional drag reduction in comparison to the typical case described above, and it may also in part explain the steeper $(PL)^{-0.6}$ decay of $C_{d,f}/C_d$ in comparison to the prediction by Henderson (2019).

In order to explain the drag augmentation that occurs for most cases with $PL < 1$, we contrast the classic drag reduction behavior to that observed for the buoyancy dominated case in Fig. 7a (which has $C_{d,f}/C_d \approx 1.6$, as seen in Fig. 8b). Here we notice that, contrary to expectations, the relative velocity (and therefore the drag force) monotonically increases from the bottom to the top of the frond. This is only possible if the frond velocity is out-of-phase with the water velocity so that $(u_x - dx/dt) > u_x$ (e.g., when $u_x > 0$, we must have $dx/dt < 0$ for this to be possible). In this case, most of the drag actually comes from the tip of the frond, and the total drag is larger than that of a rigid frond, yielding $C_{d,f}/C_d > 1$. Therefore, we conclude that drag augmentation is a physical feature of flexible vegetation that occurs when the frond motion is out-of-phase with the wave orbital velocity and it must also be taken into account. This out-of-phase motion is caused by inertial forces (note that the pressure gradient force is 90 degrees out of phase with the wave motion).

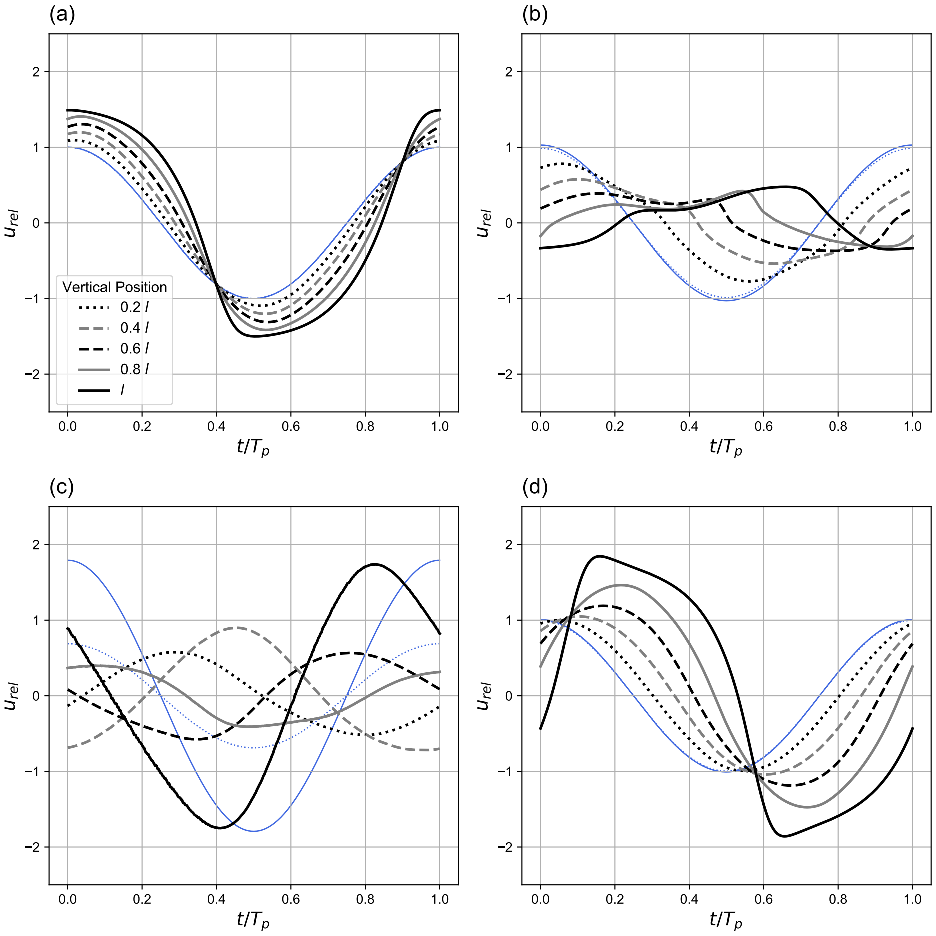

Figure 7. Relative velocities at five different locations along the length of the blade (0.2 l, 0.4 l, 0.6 l, 0.8 l, and l) over the course of one wave cycle for each case of frond motion. Solid and dotted blue lines indicate the fluid velocity at the tip of the frond and at 0.2l, respectively. All velocities are normalized by U_w. (a) Case 1: buoyancy dominated, H_s = 0.25 [m], T_p = 20 [s], l = 5 [m]. (b) Case 2: drag dominated, H_s = 2 [m], T_p = 20 [s], l = 10 [m]. (c) Case 3: inertia dominated, H_s = 0.25 [m], T_p = 5 [s], l = 10 [m]. (d) Case 4: transition, H_s = 0.25 [m], T_p = 20 [s], l = 5 [m].

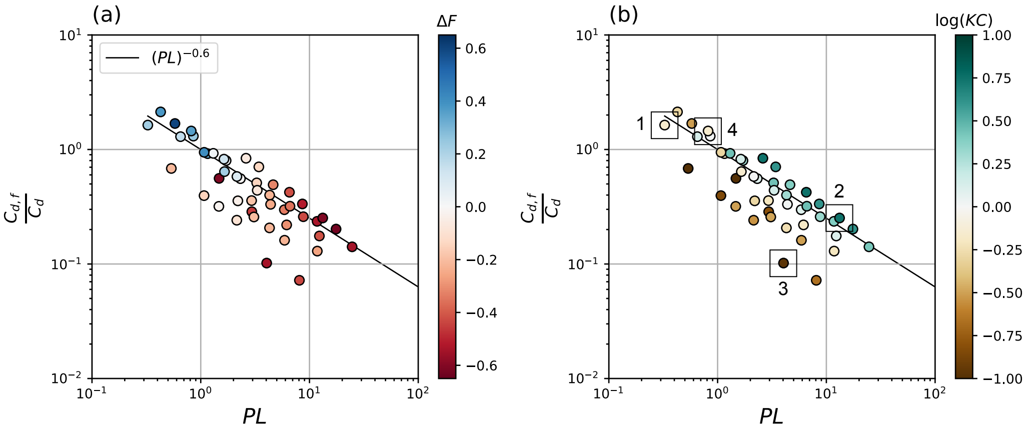

Figure 8. (a) $C_{d,f}/C_d$ versus PL, where points are colored by $\log(KC)$. Positive color values indicate $KC > 1$, while negative values represent points with $KC < 1$. (b) $C_{d,f}/C_d$ versus PL, where points are colored by $\Delta F_{D,l}$, which quantifies the difference between the drag exerted by the bottom half of the plant and the top half. Black squares 1, 2, 3, and 4 represent the same cases referenced in 3a. In both panels, the black line is the same best fit as in Fig. 6.

To further characterize this behavior, we define the parameter

$$\Delta F = \frac{[F_{D,top}]_{RMS} - [F_{D,bot}]_{RMS}}{[F_{D,top}]_{RMS} + [F_{D,bot}]_{RMS}} \quad (32)$$

where $[F_{D,top}]_{RMS}$ and $[F_{D,bot}]_{RMS}$ are the RMS of the drag integrated over the top half and bottom half of the frond. When ΔF is positive, more drag is generated by the top half of the frond than the bottom half; the opposite is true when ΔF is negative. Figure 8a shows $C_{d,f}/C_d$ against PL, but with points colored by ΔF. All the points with $C_{d,f}/C_d > 1$ have positive ΔF values, meaning that a majority of the drag is originated from the top half of the frond, thus implying out-of-phase motion between frond and water. In our most extreme case, the drag force from the upper half of the frond is almost four times as large as that of the bottom half. We have verified that all these cases with drag augmentation have relative velocity profiles similar to the one shown in Fig. 7a.

As previously discussed, the drag force decays even faster than $(PL)^{-0.6}$ in the inertia dominated cases. For the case illustrated in Fig. 7c, we see that the drag force changes sign twice between the bottom and the top of the frond. This is in part associated with the complex behavior associated with the higher natural mode that corresponds to the motion of these cases (see Fig. 4c). The large cancellations of the drag force along the frond in these cases with $KC < 1$ lead to much smaller values of the total drag in comparison to other cases. This is clearly seen in Fig.

8b, where $C_{d,f}/C_d$ is displayed against PL and colors represent their value of $\log KC$. Positive color values represent simulations where $KC > 1$, and negative color values represents simulations where $KC < 1$. There is generally a smooth decrease in KC as points move farther away from the best fit line for the large KC regime, suggesting a smooth reduction in $C_{d,f}/C_d$ with decreasing KC. As a result, this type of motion appears even more "flexible" than in the drag dominated regime. Note also that these inertia dominated cases tend to have more drag originating from the bottom of the frond or, at most, an even distribution between top and bottom drag (see Fig. 8a).

Finally, our transition case (Fig. 7d) displays a mix of traits from the three aforementioned cases, including increased drag from the upper portion of the frond due to out-of-phase motion with the water (and associated $C_{d,f}/C_d > 1$) and a switch in sign of the drag along the frond due to larger frond excursions in comparison to water parcels. For more elaboration on how to interpret Fig. 7, please refer to Figure S1 of the Supporting Information.

3.3 Asymmetric Motion

Another interesting aspect of flexible vegetation motion is the degree of asymmetry, even under symmetric wave forcing. Zhu et al. (2020) conducted an in depth analysis of the conditions for asymmetric blade motion, concluding that there are only a few conditions where blade motion is nearly symmetric: (1) when blade length is much smaller than the wavelength $\lambda = 2\pi/k$, (2) blade length is much smaller than the water depth, or (3) the water depth is much smaller than the wavelength. In our simulations, wavelengths vary between $\lambda = 37$ m and $\lambda = 210$ m, so the vast majority of our cases satisfy both (1) and (3) and we would expect symmetric frond motion. Zhu et al. (2020) quantified degree of asymmetry defining $\beta_{xT} = \overline{x}/|x_{\max}|$, where $\overline{x}$ is the average displacement over an equilibrium cycle and $|x_{\max}|$ is the maximum horizontal displacement (they also used an arbitrary threshold $\beta_{xT} < 0.05$ for nearly symmetric motion). Based on the values of $|\beta_{xT}|$ shown in Fig. 9, most of our simulations display asymmetric motion. A few of our cases with $KC \leq 1$ had negative β_{xT} values, meaning that $\overline{x}$ is slightly negative even though the wave propagates in the positive x direction. This is likely due to the effects of inertial forces being out of phase with drag. To include these points, we chose to plot the absolute value of β_{xT}.

Zhu et al. (2020) attributes the cause of asymmetric motion to be either the effect of vertical wave orbital velocities or spatial asymmetry of the encountered wave orbital velocities from

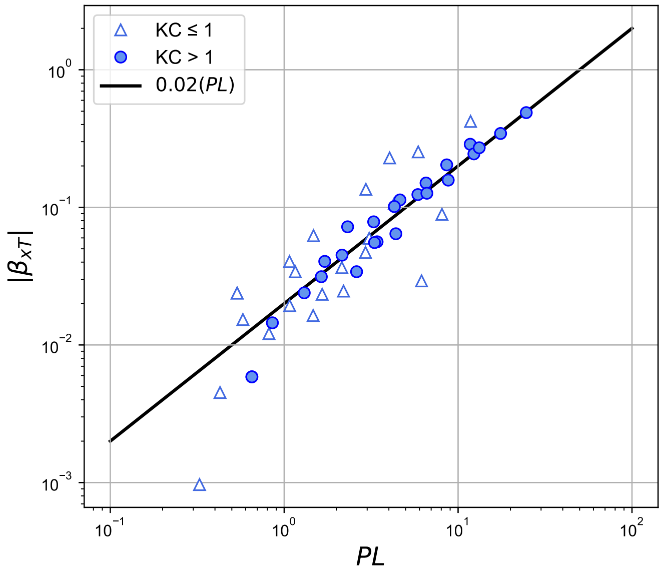

Figure 9. Degree of asymmetry, β_{xT} increases with PL. Blue filled circles are drag dominated cases ($KC > 1$); open triangles are inertia dominated ($KC \leq 1$). Black line represents the best fit for the $KC > 1$ points ($R^2 = 0.94$).

horizontal blade displacements. We performed numerical simulations removing these two effects (i.e., by setting the vertical wave velocity to zero and eliminating the forcing dependence on the x-position of the nodes) and observed only a very small reduction in the degree of asymmetry (not shown), suggesting that other mechanisms may be involved in our cases. Nevertheless, it is remarkable that the parameter PL is an excellent predictor of the degree of asymmetry measured by β_{xT}. The coefficient of determination (R^2) is larger than that for the drag coefficient reduction in Fig. 6, and even though the spread is larger for the inertia dominated cases, there seems to be no trend with KC as in the case of the drag coefficient. Note that increasing PL is mostly accomplished by increasing wave height, increasing frond length, or reducing buoyancy, conditions that are expected to lead to more asymmetric motion (Zhu et al., 2020). Importantly, the scaling of $C_{d,f}/C_d$ and β_{xT} with PL suggests that there is a correlation between drag reduction and motion asymmetry.

4 Conclusion

In this study, we developed a numerical model to investigate the motion of kelp fronds and its impact on drag forces in response to realistic monochromatic wave forcing. From the wave parameters retrieved from observations, it becomes clear that the usual assumption of weak inertial forces (i.e., large Keulegan-Carpenter number KC) is not always applicable to kelp motion in nearshore waters. A more detailed scaling analysis of the equations of frond motion suggests a 2-dimensional parameter space formed by a combination of KC, the buoyancy parameter P, and the ratio of frond length to wave horizontal excursion L. Motivated by the governing equation of motion, we chose to use PL and PL/KC as the two independent parameters. This leads to 3 asymptotic regimes (dominated by buoyancy, drag, and inertia) and successful classification of different types of frond motion (see Fig. 3).

We quantified the relative horizontal excursion of the frond in comparison to that of water, and the results shows strong dependence on KC and L. For the drag-dominated cases (large KC), frond excursion is smaller than water excursion, and differences increase with increasing KC and decreasing frond length. This is consistent with the analysis of Luhar and Nepf (2016). For the inertia dominated cases (small KC), frond excursion is larger than water excursion and differences increase with decreasing KC and frond length. Interesting, for all frond lengths, frond excursions match water excursion for $KC \approx 0.7$.

We have also investigated the extent that kelp motion impacts its drag reduction (in comparison to a rigid kelp frond). We quantify drag reduction by introducing a ratio of the true drag coefficient to that of a rigid frond $C_{d,f}/C_d$, and found that drag reduction is a function of KC and PL. Our empirical fit to simulation results yields

$$C_{d,f}/C_d = \begin{cases} (PL)^{-0.6} & \text{if } KC > 1 \\ 0.7(PL)^{-0.8} & \text{if } KC \leq 1 \end{cases} \tag{33}$$

The result for the drag dominated regime ($KC > 1$) is fairly close to the prediction by Henderson (2019). The steeper drag reduction with PL in the inertia dominated case ($KC \leq 1$) results from a reversal of the drag direction along the frond and cancellation between drag forces acting in opposite directions. We also observe drag augmentation (i.e., $C_{d,f}/C_d > 1$) for cases in which $PL < 1$, and track the origin of this to the motion of the frond being out-of-phase with the motion of the water.

It is important to note that drag reduction is directly associated with the efficiency of wave energy dissipation by the vegetation. As a general conclusion, in the regimes of frond motion studied here, the effective drag coefficient is reduced with increasing PL and decreasing KC. Waves with smaller periods correspond to smaller KC and larger PL, and thus smaller drag coefficient and less efficient energy dissipation. Similarly, increasing wave height increases PL (without affecting KC), leading to smaller drag.

Future research needs to extend the modeling to include effects of mean currents and broadband wave spectra (and possibly turbulence) on the frond motion, and the presence of surface canopies. In addition, observational confirmation by synchronous measurements of wave and kelp motions are necessary to validate our modeling results.

Appendix A Model Validation

Due to lack of detailed observations of blade/frond motion and drag reduction for cases with negligible bending stiffness that could be used to validate our model assumptions, we test our model against the theory developed by Luhar and Nepf (2011) for bending of flexible blades in steady unidirectional flow. More specifically, we compare model results to the predictions of effective length given by their Equation 16, which includes both bending stiffness and buoyancy as restoring forces and can be written in terms of P as

$$\frac{l_e}{l} = 1 - \frac{1 - 0.9Ca^{-1/3}}{1 + 8Ca^{-3/2} + P^{-3/2}}. \tag{A1}$$

Note that this theory-based expression has empirical constants. We made small adjustments to our numerical model to better match the conditions used in Luhar and Nepf (2011). We modified the drag force to include the frontal area reduction due to blade bending (i.e., including the $\cos\theta$ term), and removed the drag force in the z direction (the relative velocity being defined only based on the x component).

Our goal is to test the hypothesis that, for our range of values of Ca and P, neglecting the bending stiffness (i.e., assuming $Ca \rightarrow \infty$) has a negligible effect on the results. Our study design uses all the kelp geometric and constitutive properties described in Section 2.2, neglecting the bending stiffness and still allowing for stretching of the blade. We tested model performance across a wide range of P by varying current velocity while holding buoyancy constant via kelp density. Results are shown in Fig. A1.

The effective length predicted by our model compares well to the results from Eq. (A1) across the entire range of P (Fig. A1a). The fractional error in predictions (Fig. A1b) is always below 10% for the range of P in our wave simulations ($0.01 < P < 4$). In addition to our neglect of bending stiffness, differences could also originate from the error between the simulations in Luhar and Nepf (2011) and their fitted equation, and also our inclusion of frond stretching. We note that

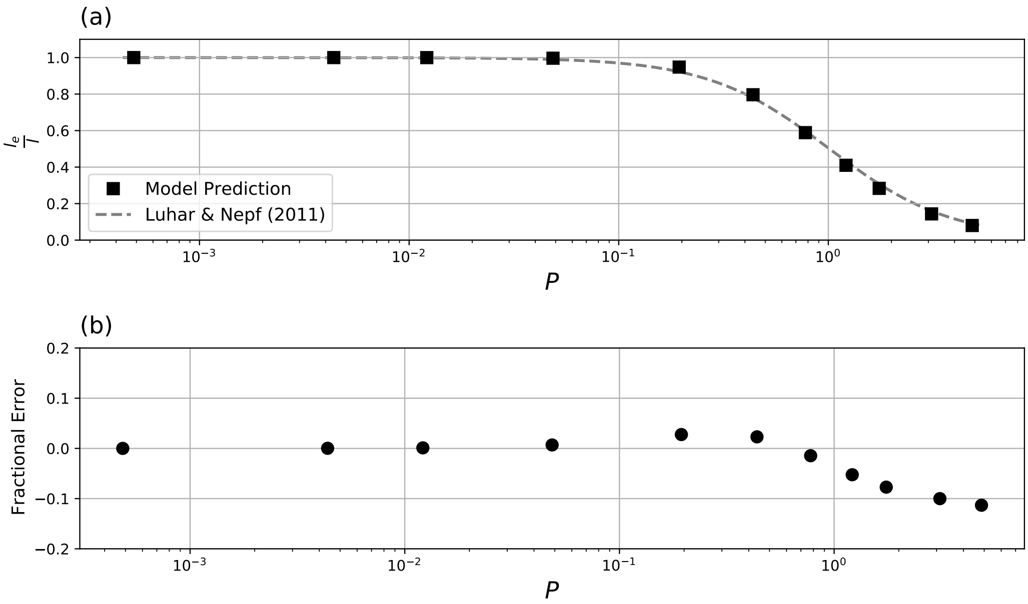

Figure A1. (a) Model predictions of effective length (black squares) compared to the model from Luhar and Nepf (2011) given by Eq. (A1) (dashed gray line). (b) Fractional error of present model predictions.

comparing Eq. (A1) including and neglecting Ca leads to errors of only up to 3% for the range of conditions used in our model. Therefore, despite the differences between blade response to a steady flow and our study of unsteady wave motion, we conclude that the errors incurred by neglecting bending stiffness in our numerical model are likely minor and would not impact the overall conclusions of our study.

Open Research Section

The data required to reproduce the figures will be made available at a public repository prior to final publication.

Acknowledgments

The authors report no conflict of interest.

This work is supported by the ARPA-E MARINER Program (DE-AR0000920). JFM also gratefully acknowledges support by the Sharon Fisher Endowment and the Norton Rodman Endowment (Undergraduate Research Scholars Program, UCLA Undergraduate Research Center – Sciences), and the Queen's Road Fellowship Program (with special thanks to its founder, Fritz Demopoulos).

Wave data were furnished by the Coastal Data Information Program (CDIP), Integrative Oceanography Division, operated by the Scripps Institution of Oceanography, under the sponsorship of the U.S. Army Corps of Engineers and the California Department of Parks and Recreation (`https://doi.org/10.18437/C7WC72`).

References

Abbott, I. A., & Hollenberg, G. J. (1992). *Marine algae of california*. Stanford University Press.

Dayton, P. K., Currie, V., Gerrodette, T., Keller, B. D., Rosenthal, R., & Tresca, D. V. (1984). Patch dynamics and stability of some california kelp communities. *Ecological Monographs*, *54*(3), 253–289. https://doi.org/10.2307/1942498

Dean, R. G., & Dalrymple, R. A. (1991). *Water wave mechanics for engineers and scientists* (Vol. 2). World Scientific Publishing Company. https://doi.org/10.1142/1232

Denny, M. W., Gaylord, B. P., & Cowen, E. A. (1997). Flow and flexibility ii. the roles of size and shape in determining wave forces on the bull kelp nereocystis luetkeana. *Journal of Experimental Biology*, *200*(24), 3165–3183. https://doi.org/10.1242/jeb.200.24.3165

Eger, A. M., Marzinelli, E. M., Beas-Luna, R., Blain, C. O., Blamey, L. K., Byrnes, J. E., ... others (2023). The value of ecosystem services in global marine kelp forests. *Nature Communications*, *14*(1), 1894. https://doi.org/10.1038/s41467-023-37385-0

Elwany, M. H. S., O'Reilly, W. C., Guza, R. T., & Flick, R. E. (1995). Effects of southern california kelp beds on waves. *Journal of Waterway, Port, Coastal, and Ocean Engineering*, *121*(2), 143–150. https://doi.org/10.1061/(ASCE)0733-950X(1995)121:2(143)

Frieder, C. A., Yan, C., Chamecki, M., Dauhajre, D., McWilliams, J. C., Infante, J., ... Davis, K. A. (2022). A macroalgal cultivation modeling system (macmods): evaluating the role of physical-biological coupling on nutrients and farm yield. *Frontiers in Marine Science*, *9*. https://doi.org/10.3389/fmars.2022.752951

Froehlich, H. E., Afflerbach, J. C., Frazier, M., & Halpern, B. S. (2019). Blue growth potential to mitigate climate change through seaweed offsetting. *Current Biology*, *29*(18), 3087–3093. https://doi.org/10.1016/j.cub.2019.07.041

Gao, G., Gao, L., Jiang, M., Jian, A., & He, L. (2021). The potential of seaweed cultivation to achieve carbon neutrality and mitigate deoxygenation and eutrophication. *Environmental Research Letters*, *17*(1), 014018. https://doi.org/10.1088/1748-9326/ac3fd9

Gaylord, B., Denny, M. W., & Koehl, M. A. (2003). Modulation of wave forces on kelp canopies by alongshore currents. *Limnology and Oceanography*, *48*(2), 860–871. https://doi.org/10.4319/lo.2003.48.2.0860

Gaylord, B., Rosman, J. H., Reed, D. C., Koseff, J. R., Fram, J., MacIntyre, S., . . . others (2007). Spatial patterns of flow and their modification within and around a giant kelp forest. *Limnology and Oceanography*, *52*(5), 1838–1852. https://doi.org/10.4319/lo.2007.52.5.1838

Henderson, S. M. (2019). Motion of buoyant, flexible aquatic vegetation under waves: simple theoretical models and parameterization of wave dissipation. *Coastal Engineering*, *152*, 103497. https://doi.org/10.1016/j.coastaleng.2019.04.009

Hoegh-Guldberg, O., Lovelock, C., Caldeira, K., Howard, J., Chopin, T., & Gaines, S. (2019). The ocean as a solution to climate change: five opportunities for action.

Jackson, G. A., & Winant, C. D. (1983). Effect of a kelp forest on coastal currents. *Continental Shelf Research*, *2*(1), 75–80. https://doi.org/10.1016/0278-4343(83)90023-7

Johnson, A. S., & Koehl, M. A. R. (1994). Maintenance of dynamic strain similarity and environmental stress factor in different flow habitats: thallus allometry and material properties of a giant kelp. *Journal of Experimental Biology*, *195*(1), 381–410. https://doi.org/10.1242/jeb.195.1.381

Journee, J., & Massie, W. (2000). *Offshore hydromechanics* (Vol. 1). CITG Section Hydraulic Engineering.

Kain, J. M., & Dawes, C. (1987). Useful european seaweeds: past hopes and present cultivation. *Hydrobiologia*, *151*, 173–181. https://doi.org/10.1007/BF00046124

Keulegan, G. H., & Carpenter, L. H. (1956). *Forces on cylinders and plates in an oscillating fluid*. National Bureau of Standards.

Lei, J., & Nepf, H. M. (2019). Wave damping by flexible vegetation: Connecting individual blade dynamics to the meadow scale. *Coastal Engineering*, *147*, 138–148. https://doi.org/10.1016/j.coastaleng.2019.01.008

Luhar, M., & Nepf, H. M. (2011). Flow-induced reconfiguration of buoyant and flexible aquatic vegetation. *Limnology and Oceanography*, *56*(6), 2003–2017. https://doi.org/10.4319/lo.2011.56.6.2003

Luhar, M., & Nepf, H. M. (2016). Wave-induced dynamics of flexible blades. *Journal of Fluids and Structures*, *61*, 20–41. https://doi.org/10.1016/j.jfluidstructs.2015.11.007

Marjoribanks, T. I., Hardy, R. J., Lane, S. N., & Parsons, D. R. (2014). High-resolution numerical modelling of flow—vegetation interactions. *Journal of Hydraulic Research*, *52*(6), 775–793. https://doi.org/10.1080/00221686.2014.948502

Milledge, J. J., Smith, B., Dyer, P. W., & Harvey, P. (2014). Macroalgae-derived biofuel: a review of methods of energy extraction from seaweed biomass. *Energies*, *7*(11), 7194–7222. https://doi.org/10.3390/en7117194

Monismith, S., Alnajjar, M., Daly, M., Valle-Levinson, A., Juarez, B., Fagundes, M., . . . Woodson, C. B. (2022). Kelp forest drag coefficients derived from tidal flow data. *Estuaries and Coasts*, *45*(8), 2492–2503. https://doi.org/10.1007/s12237-022-01098-2

Mullarney, J. C., & Henderson, S. M. (2010). Wave-forced motion of submerged single-stem vegetation. *Journal of Geophysical Research: Oceans*, *115*(C12). https://doi.org/10.1029/2010JC006448

Mullarney, J. C., & Pilditch, C. A. (2017). The differential response of kelp to swell and infragravity wave motion. *Limnology and Oceanography*, *62*(6), 2524–2537. https://doi.org/10.1002/lno.10587

Nikora, V., Goring, D., & Biggs, B. (1998). A simple model of stream periphyton-flow interactions. *Oikos*, *81*, 607–611. https://doi.org/10.2307/3546782

Peteiro, C. (2018). Alginate production from marine macroalgae, with emphasis on kelp farming. *Alginates and Their Biomedical Applications*, *11*, 27–66. https://doi.org/10.1007/978-981-10-6910-9_2

Razmi, A. M., Chamecki, M., & Nepf, H. M. (2020). Efficient numerical representation of the impacts of flexible plant reconfiguration on canopy posture and hydrodynamic drag. *Journal of Hydraulic Research*, *58*(5), 755–766. https://doi.org/10.1080/00221686.2019.1671511

Rosman, J. H., Denny, M. W., Zeller, R. B., Monismith, S. G., & Koseff, J. R. (2013). Interaction of waves and currents with kelp forests (macrocystis pyrifera): Insights from a dynamically scaled laboratory model. *Limnology and Oceanography*, *58*(3), 790–802. https://doi.org/10.4319/lo.2013.58.3.0790

Sarpkaya, T., & O'Keefe, J. L. (1996). Oscillating flow about two and three-dimensional bilge keels. *Journal of Offshore Mechanics and Arctic Engineering*, *118*(1), 1–6. https://doi.org/10.1115/1.2828796

Schiel, D. R., & Foster, M. S. (2015). *The biology and ecology of giant kelp forests*. University of California Press.

Seymour, R., Tegner, M., Dayton, P., & Parnell, P. (1989). Storm wave induced mortality of giant kelp, macrocystis pyrifera, in southern california. *Estuarine, Coastal and Shelf Science*, *28*(3), 277–292. https://doi.org/10.1016/0272-7714(89)90018-8

Thornton, T. F. (2015). The ideology and practice of pacific herring cultivation among the tlingit and haida. *Human Ecology*, *43*, 213–223. https://doi.org/10.1007/s10745-015-9736-2

Utter, B. D., & Denny, M. W. (1996). Wave-induced forces on the giant kelp macrocystis pyrifera (agardh): field test of a computational model. *Journal of Experimental Biology*, *199*(12), 2645–2654. https://doi.org/10.1242/jeb.199.12.2645

Vogel, S. (1984). Drag and flexibility in sessile organisms. *American Zoologist*, *24*(1), 37–44. https://doi.org/10.1093/icb/24.1.37

Zeller, R. B., Weitzman, J. S., Abbett, M. E., Zarama, F. J., Fringer, O. B., & Koseff, J. R. (2014). Improved parameterization of seagrass blade dynamics and wave attenuation based on numerical and laboratory experiments. *Limnology and Oceanography*, *59*(1), 251–266. https://doi.org/10.4319/lo.2014.59.1.0251

Zhu, L., Zou, Q.-P., Huguenard, K., & Fredriksson, D. W. (2020). Mechanisms for the asymmetric motion of submerged aquatic vegetation in waves: a consistent-mass cable model. *Journal of Geophysical Research: Oceans*, *125*(2). https://doi.org/10.1029/2019JC015517

Wave-Induced Motion and Drag Reduction of Kelp

Jayde F. Meng[1], **Marcelo Chamecki**[1]

[1]Department of Atmospheric and Oceanic Sciences, University of California, Los Angeles, CA 90025, USA

Key Points:

- A 2D parameter space is proposed to characterize dominant forces and classify different types of kelp motion
- Inertial forces can significantly impact frond motion and drag reduction, and even lead to drag augmentation (compared to rigid fronds)
- We provide empirical fits to quantify drag reduction/augmentation in low- and high-inertia conditions

Corresponding author: Marcelo Chamecki, `chamecki@ucla.edu`

Abstract

It is well known that the motion of flexible vegetation leads to drag reduction in comparison to rigid vegetation. In this study, we use a numerical model to investigate how the detailed motion of kelp fronds in response to forcing by surface gravity waves can impact the drag exerted by the kelp on waves. We find that this motion can be characterized in terms of three dimensionless numbers: (1) the ratio of hydrodynamic drag to buoyancy, (2) the ratio of blade length to wave excursion, and (3) the Keulegan-Carpenter number, which measures the ratio of drag to inertial forces. We quantify drag reduction, and find that inertial forces can significantly impact the amplitude of kelp motion and amount of kelp drag reduction. Under certain wave conditions, inertial forces can cause kelp fronds to accelerate more quickly relative to the wave, which can lead to increased drag reduction and reduced wave energy dissipation. In some conditions, frond motion leads to drag augmentation in comparison to rigid fronds. Additionally, we discuss other features of kelp motion, such as the degree of asymmetry, and their relationship with enhanced drag reduction.

Plain Language Summary

We use a numerical model to study how kelp fronds move in response to passing ocean waves. Flexible motion reduces the drag forces experienced by the kelp and increases survival in extreme conditions such as energetic waves. Frond motion also reduces the amount of wave energy dissipation. The type of motion that the fronds undergo in response to different types of waves is determined by the dominant forces, and so is the amount of drag reduction. Our findings show that, unlike other types of aquatic vegetation, inertial forces (e.g. due to the pressure variations in the water) can be as important as (and sometimes more important) than the drag forces caused by the flow.

1 Introduction

Macroalgae species, such as kelp, are integral to the health of many coastal ecosystems. Kelp forests help preserve biodiversity by serving as habitats and food sources for different marine species (Dayton et al., 1984; Schiel & Foster, 2015). Kelp forests also help remediate anthropogenic changes, by mitigating eutrophication pollution through nitrate removal (Gao et al., 2021) and reducing ocean acidification and offsetting carbon dioxide emissions via carbon sequestration (Froehlich et al., 2019; Hoegh-Guldberg et al., 2019). Globally, kelp forests generate an average of $500 billion a year in terms of ecosystem services (Eger et al., 2023).

Moreover, kelp harvesting is central to numerous local economies. Many cultures around the world have a rich history of relying on kelp as a food source, a way to enhance fisheries, a fertilizer for soil, etc. (Thornton, 2015; Kain & Dawes, 1987). More recently, alginate sourced from kelp has also been utilized as an important additive in pharmaceutical and biomedical industries (Peteiro, 2018). Furthermore, the high energy content and fast growth rates of kelp have singled them out to be a potential source of biofuel that does not compete for space with land-grown crops for the food industry (Milledge et al., 2014; Frieder et al., 2022).

With all of these benefits, it is critical to understand how we can sustainably support the growth and maintenance of kelp forests and farms. In particular, we are interested in the hydrodynamic interactions between kelp and ocean waves. This study focuses primarily on the hydrodynamics of the kelp species *Macrocystis pyrifera*, more commonly known as giant kelp. Giant kelp is native to the coasts of California and is particularly well-suited for the purposes of farming due to its fast growth rates (up to 0.5 meters per day). They are the largest species of algae and can reach lengths of 20 meters or more (Abbott & Hollenberg, 1992).

This type of kelp is made up of dozens of fronds attached to a holdfast, which keeps the kelp anchored to the substrate. Each frond consists of a stem-like stipe and leaf-like blades, and at the base of each blade is a pneumatocyst, or a gas-filled bladder. These pneumatocysts allow *M. pyrifera* to be highly buoyant. Giant kelp stipes also have relatively low rigidity compared to seagrasses, allowing stipes to easily bend in response to hydrodynamic forces. A diagram of kelp physiology is given in Fig. 1(a).

Many past observational studies on *M. pyrifera* (henceforth simply referred to as kelp) hydrodynamics have focused on quantifying the bulk effects of kelp on the flow. The drag force imparted by the kelp on the currents reduces flow rates through kelp forests (Jackson & Winant, 1983; Gaylord et al., 2007). For example, Monismith et al. (2022) estimated the scaling for kelp forest drag coefficient in tidal flows via biomass relationships. Laboratory studies have also shown that the presence of kelp modifies wave orbital velocities (Rosman et al., 2013). However, kelp forests generally dissipate minimum amounts of wave energy due to its highly flexible nature (Elwany et al., 1995).

Because of its nearshore environment, kelp are especially sensitive to the forces caused by surface gravity waves (Gaylord et al., 2003). High energy wave amplitudes can cause kelp stipes to break and entangle, or even dislodge fronds from their holdfast (Seymour et al., 1989; Dayton et al., 1984). Kelp fronds have also been observed to respond differently to waves with different periods (Mullarney & Pilditch, 2017). Generally, flexibility is a strategy employed by seagrasses and algae to reduce drag forces and increase survivability in high-flow environments (Vogel, 1984; Utter & Denny, 1996). In return, the drag exerted on the waves by kelp is highly dependent on the detailed motion of the kelp frond. Thus, the two-way interaction between flexible kelp fronds and waves impact both, the survivability of kelp and the physical properties of the waves.

Numerical models have also been used to predict the forces that individual kelp fronds undergo in different wave conditions, and thus, how likely they are to survive. For example, Jackson and Winant (1983) modeled kelp stipes as rigid vertical columns, while Utter and Denny (1996) represented kelp fronds as buoys attached to a flexible rope and predicted kelp survivability rates under different wave conditions. They model a single point element where hydrodynamic forces such as buoyancy, drag, and pressure gradient forces are countered by tension (Utter & Denny, 1996; Denny et al., 1997).

Additionally, a number of more sophisticated numerical models have been developed to investigate submerged aquatic vegetation motion under wave conditions, including but not limited to variations of the Euler-Bernoulli beam model utilized by Marjoribanks et al. (2014), Zeller et al. (2014), and Luhar and Nepf (2016). Zhu et al. (2020) expanded on this work and developed a consistent-mass cable model to study asymmetric motion of aquatic vegetation. However, these models have not been applied to the study of giant kelp, in part because they suffer from numerical stability issues in cases with low bending stiffness (Zeller et al., 2014).

A major thrust of theoretical and numerical studies is to develop understanding and quantification of how plant motion affects drag reduction. For instance, Luhar and Nepf (2011) developed a scaling model for the drag of smaller seagrasses in currents by considering the different balances between drag, buoyancy, and rigidity. Luhar and Nepf (2016) and Lei and Nepf (2019) extended this work to wave conditions and the meadow scale, mainly focusing on seagrasses for which hydrodynamic forcing is primarily balanced by blade stiffness. Henderson (2019) complemented this work by also analyzing drag reduction in plants where drag forces are balanced by both stiffness and buoyancy.

Notably, most of the past work has been conducted with the assumption of drag dominated flows; that is, inertial forces such as the pressure gradient and added mass forces are insignificant when compared to drag forces and do not contribute much to plant motion. This is relatively accurate for smaller seagrass species, which usually grow in very shallow waters. However, kelp often grows in deeper waters and fronds can be quite long. Furthermore, typical wave conditions of coastal California create a natural environment where inertial forces become important. Together, all of these factors (longer plant lengths, the importance of inertial forces, the predominance of buoyancy over bending stiffness as a restoring force) produce distinct dynamical behavior and lead to different laws of drag reduction.

Thus, the purpose of this study is to gain a better understanding of kelp hydrodynamics by investigating the impact of inertial forces on kelp motion and consequently, kelp drag reduction. We first develop a generalized numerical model for kelp frond motion, and the model is then used to study the response of kelp fronds to different wave conditions observed on the coast of California. We focus specifically on the importance of inertial forces and how that impacts different aspects of frond motion and drag reduction.

2 Methods

2.1 Model Description

We constructed a two dimensional model for the motion of an individual kelp frond following the approach outlined by Rosman et al. (2013) and Marjoribanks et al. (2014), which can be considered as a refinement of the simple tethered-buoy model developed by Utter and Denny (1996). The kelp frond is discretized into n segments, and each segment is modeled as a point mass attached to a string with the flexibility and tensile stiffness of kelp stipes. Thus, the kelp frond is modeled as a set of point masses connected by strings. The position of each point mass is represented by the vector $\mathbf{x}_i = (x_i, z_i)$, and its velocity by the vector $d\mathbf{x}_i/dt$. A visualization of this representation is given in Fig. 1(b). Note that kelp usually grows to form a dense canopy floating on the surface that can significantly enhance the total drag (Rosman et al., 2013). For simplicity, we do not consider the presence of the surface canopy here, and focus only on situations in which the frond length is smaller than the water depth.

The motion of each point mass is governed by Newton's second law. Following Utter and Denny (1996), Denny et al. (1997), and Rosman et al. (2013), we use Morison's equation (e.g., see Journee & Massie, 2000) to describe the forces acting on kelp. In the present model, we included the five main forces that determine kelp motion: buoyancy, drag, added mass, pressure gradient, and tension. We assume that the drag is exerted by the area of the blades, the bending stiffness originates from the kelp stipe, and the buoyancy comes from the pneumatocysts. Because kelp stipes are very flexible, we assume that their rigidity, or resistance to bending, is negligible. As in Utter and Denny (1996), we also neglect lift and skin friction forces, which are rel-

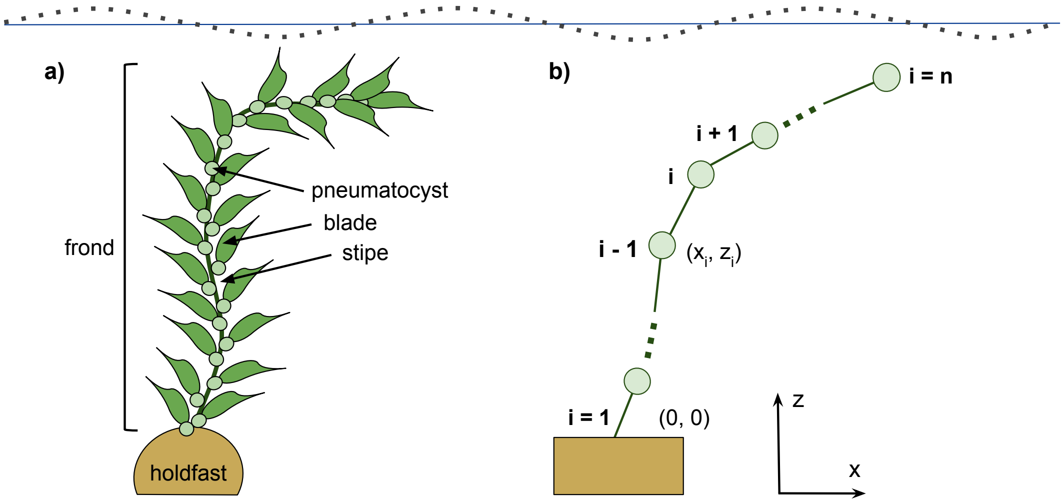

Figure 1. (a) *M. pyrifera* frond and (b) schematic of the discretization of the frond in the numerical model.

atively inconsequential. Assuming each segment has an effective mass m_k, the governing equation of motion for the i^{th} segment is given by

$$m_k \frac{d^2\mathbf{x}_i}{dt} = \mathbf{F}_{D,i} + \mathbf{F}_{B,i} + \mathbf{F}_{P,i} + \mathbf{F}_{AM,i} + \mathbf{F}_{T,i} + \mathbf{F}_{T,i+1}, \tag{1}$$

where $\mathbf{F}_{D,i}$ is the drag force, $\mathbf{F}_{B,i}$ is the buoyant force, $\mathbf{F}_{P,i}$ is the pressure gradient force, $\mathbf{F}_{AM,i}$ is the added mass force, and $\mathbf{F}_{T,i}$ and $\mathbf{F}_{T,i+1}$ are the tension forces on the strings that connect the point mass to its neighboring masses.

The drag force is modeled using a quadratic equation given in terms of relative velocity

$$\mathbf{F}_{D,i} = \frac{1}{2}\rho_w C_d A_i \left|\mathbf{u}_i - \frac{d\mathbf{x}_i}{dt}\right| \left(\mathbf{u}_i - \frac{d\mathbf{x}_i}{dt}\right), \tag{2}$$

where ρ_w is the density of seawater, C_d is the drag coefficient, A_i is the maximal projected area of each frond segment, and $\mathbf{u}_i = (u_{x,i}, u_{z,i})$ is the two-dimensional fluid velocity vector. Contrary to most models of seagrass dynamics (Luhar & Nepf, 2011, 2016), we assume that there is no reduction in exposed area with bending. This is because as kelp fronds bend, their blades remain oriented with the flow, so the exposed area changes very little (e.g., the contribution of the area of the stipe to the drag force is negligible).

The buoyancy force is given by

$$\mathbf{F}_{B,i} = (\rho_k - \rho_w)V_i\mathbf{g}, \tag{3}$$

where ρ_k is the density of the kelp frond, V_i is the volume of each segment, and $\mathbf{g}$ is the gravitational acceleration vector.

Two forces are associated with the acceleration of the fluid: the pressure gradient force (or Froude-Krylov force) and the added mass force. They are given, respectively, by

$$\mathbf{F}_{P,i} = \rho_w V_i \frac{\partial \mathbf{u}_i}{\partial t} \tag{4}$$

and

$$\mathbf{F}_{AM,i} = C_a \rho_w V_i \left(\frac{\partial \mathbf{u}_i}{\partial t} - \frac{d^2 \mathbf{x}_i}{dt} \right), \tag{5}$$

where C_a is the added mass coefficient. We will refer to these two forces as the inertial forces acting on the kelp frond.

In oscillatory flows, it is typical to model the drag and added mass coefficients (C_d and C_a) as a function of the Keulegan-Carpenter number (KC), which characterizes the ratio between inertial and drag forces (e.g., see Luhar & Nepf, 2016). This is done based on experiments with flat plates and similar objects in oscillatory flow (Keulegan & Carpenter, 1956; Sarpkaya & O'Keefe, 1996), for which $KC = U_w T_p / d$, where U_w is a characteristic velocity scale, T_p is the wave period, and d is the thickness of the plate. These effects are attributed to the vortex shedding from these blunt objects and there is little reason to believe that kelp fronds have a similar behavior. Therefore, we do not include explicit effects of KC on C_d and C_a in our model.

Each point mass is also subject to tension forces from the string connected to the point mass below, $\mathbf{F}_{T,i}$, and to the point mass above, $\mathbf{F}_{T,i+1}$. Thus, the total tension force on each segment is given by the sum of the two tensions, or

$$\mathbf{F}_{T,i} + \mathbf{F}_{T,i+1} = -EA_c \frac{|\mathbf{x}_i - \mathbf{x}_{i-1}| - l_i}{l_i} \mathbf{e}_{s,i} + EA_c \frac{|\mathbf{x}_{i+1} - \mathbf{x}_i| - l_{i+1}}{l_{i+1}} \mathbf{e}_{s,i+1}, \tag{6}$$

when $|\mathbf{x}_i - \mathbf{x}_{i-1}| > l_i$ and $|\mathbf{x}_{i+1} - \mathbf{x}_i| > l_{i+1}$, where l_i and l_{i+1} are the lengths of each segment. Here we have adopted the elastic model used by Utter and Denny (1996) to represent the tension on the string, and E is the modulus of elasticity of the kelp, while $\mathbf{e}_{s,i}$ and $\mathbf{e}_{s,i+1}$ are the unit vectors in the direction of their respective segments. We assume that $\mathbf{F}_{T,i} = 0$ at the tip of the frond (last segment, $i = n$), and that the plant is rooted at $\mathbf{x}_0 = (0, 0)$. Note that by adopting this model and solving for the tension force explicitly, our model allows for stretching and compression of each frond segment.

The complete equation after dividing all terms by the total volume occupied by each kelp segment is

$$\begin{aligned}(\rho_k + C_a \rho_w) \frac{d^2 \mathbf{x}_i}{dt} = \; & \tfrac{1}{2} \rho_w C_d \tfrac{A_i}{V_i} \left| \mathbf{u}_i - \tfrac{d\mathbf{x}_i}{dt} \right| \left(\mathbf{u}_i - \tfrac{d\mathbf{x}_i}{dt} \right) + (\rho_k - \rho_w) \mathbf{g} + (\rho_w + C_a \rho_w) \tfrac{\partial \mathbf{u}_i}{\partial t} \\ & + \tfrac{EA_c}{V_i} \left(-\tfrac{|\mathbf{x}_i - \mathbf{x}_{i-1}| - l_i}{l_i} \mathbf{e}_{s,i} + \tfrac{|\mathbf{x}_{i+1} - \mathbf{x}_i| - l_{i+1}}{l_{i+1}} \mathbf{e}_{s,i+1} \right)\end{aligned} \tag{7}$$

where the effective mass m_k is given by $V_i(\rho_k + C_a \rho_w)$. The set of equations (7) is numerically integrated in time using a fourth-order Runge-Kutta algorithm to solve for the position of all point masses $\mathbf{x}_i = (x_i, z_i)$ and associated velocities. In our current model implementation, all the segment have the same geometrical properties such that A_i, l_i, and V_i are all constant for all i.

The main differences between our modeling approach and the more standard models used for seagrass (e.g., Marjoribanks et al., 2014; Zeller et al., 2014; Luhar & Nepf, 2016) are that: (1) we neglect bending stiffness given that the restoring force to resist motion in kelp is mostly provided by the buoyancy force, and models that include bending stiffness for low stiffness systems generate numerical instability issues such as poor convergence (Zeller et al., 2014); (2) we allow for elastic stretching deformation instead of imposing a constant frond length, which is important in modeling kelp motion (Johnson & Koehl, 1994; Utter & Denny, 1996). As an aside, we attempted to use the model developed by (Luhar & Nepf, 2016) to simulate some of our cases, but ran into numerical instability issues even for the shortest fronds under the least energetic wave conditions despite using a very fine grid resolution and small time step.

2.2 Model Setup

We study frond motion by imposing a two-dimensional linear wave flow field represented by $\mathbf{u} = (u_x, u_z)$. For a coordinate system located at the bottom of the ocean, the wave orbital velocity components at a location (x, z) are given by (Dean & Dalrymple, 1991):

$$\begin{cases} u_x = A_w \omega \dfrac{\cosh(kz)}{\sinh(kH)} \cos(kx - \omega t) \\ u_z = A_w \omega \dfrac{\sinh(kz)}{\sinh(kH)} \sin(kx - \omega t) \end{cases} \tag{8}$$

where A_w is the wave amplitude, ω is the wave frequency, k is the wavenumber, and $H = 12$ m is the depth of the water column (note that in this coordinate system, $z = H$ at the surface).

To investigate the motion of kelp in its natural habitat, we utilized buoy data from the Coastal Data Information Program (CDIP; `https://cdip.ucsd.edu`). More specifically, buoys 87, 88, and 89 recorded local wave conditions in real kelp forests along the coast of the Channel Islands (Santa Rosa and Santa Cruz Islands) from October 1995 through December 1995. We used their measurements of significant wave height, H_s, and peak wave period, T_p, to determine typical wave conditions within natural kelp forests on the California coast. The joint probability density function of measured significant wave height and wave period is shown in Fig. 2. In total, we selected sixteen different wave conditions covering the full realistic range of observed waves. For the simple monochromatic wave model, we approximated the wave amplitude as $A_w = H_s/2$ and cal-

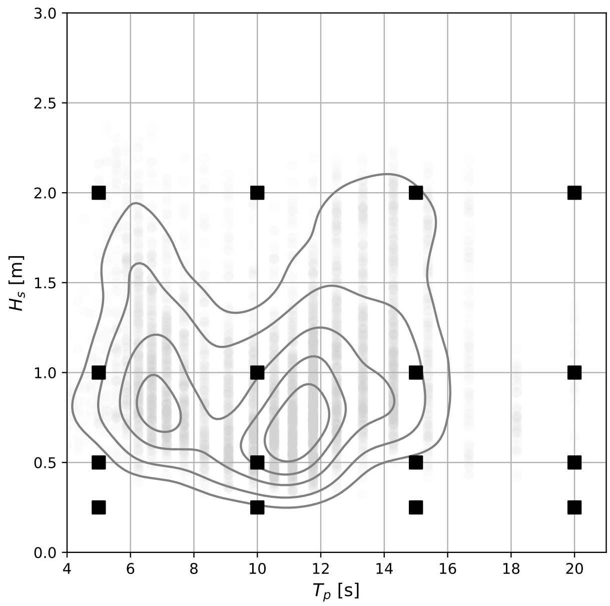

Figure 2. Simulated wave conditions. Light gray circles represent the aggregated CDIP measurements, and the gray lines represent the probability density function of the data (levels: 0.1, 0.25, 0.5, 0.75, 0.9). Black squares represent the conditions we selected for our runs. Data from CDIP, Scripps Institution of Oceanography.

culated the wave frequency from $\omega = 2\pi/T_p$ and the wave number from the dispersion relation $\omega = \sqrt{gk \tanh(kH)}$. The resulting waves fall in the range of $1/3 < kH < 2$, so we avoid using approximations for deep-water or shallow-water waves.

The kelp properties used in the model were mostly compiled from Utter and Denny (1996), and these values are presented in Table 1. Here, the kelp density ρ_k is supposed to represent the bulk density of the frond, including the gas-filled pneumatocysts. The value adopted here was obtained from Rosman et al. (2013) and was confirmed from measurements of frond mass and volume (K. A. Davis unpubl.). Notably, this is about 40% larger than the value adopted by Henderson (2019). The drag coefficient adopted here is from the intercept of the drag-velocity plot by Utter and Denny (1996) (i.e., the drag for a rigid frond), and it is in good agreement with the mode of the distribution obtained by Monismith et al. (2022) for intermediate biomass kelp forests. Finally, we obtained an estimate of frond volume indirectly from the frond projected area, the average mass per unit area, and the frond density.

Table 1. List of kelp properties and their associated variables and values. All values are from (Utter & Denny, 1996), except for ρ_k which is taken from (Rosman et al., 2013).

Variable	Description	Value
ρ_k	Density of kelp	850 [kg m^{-3}]
ρ_w	Density of seawater	1025 [kg m^{-3}]
C_a	Added mass coefficient	3
C_d	Drag coefficient	0.0148
l	Frond length	2, 5, 10 [m]
A	Maximal projected area of a frond	$0.297 \times l^{0.955}$ [m^2]
A_c	Cross-sectional area of a stipe	4.1×10^{-5} [m^2]
M_A	Average mass per unit area	0.774 [kg m^2]
V	Estimated volume of frond	$V = \frac{M_A A}{\rho_k}$ [m^3]
E	Modulus of elasticity	1.91×10^7 [Pa]

For each of the sixteen wave parameters, we tested three different frond lengths: 2 m, 5 m, and 10 m. Because kelp fronds can grow to be quite large, these lengths were selected in order to illustrate how kelp behaves in different wave conditions over its entire life cycle. This combination of plant length and wave conditions resulted in 48 simulations (see Table 2). Out of these cases, there were two that showed unrealistic amounts of stretching and compression (i.e. larger than 1% of the frond length) due to the elasticity of the kelp stipe: (1) $l = 10$ m, $H_s = 1$ m, $T_p = 5$ s; (2) $l = 10$ m, $H_s = 2$ m, $T_p = 5$ s. Thus, we removed these two cases from further analysis. The wave conditions in the removed cases are exceptionally high energy, and rarely occur in the real world (see Fig. 2). We postulate that realistically, kelp fronds would probably become dislodged in those extreme, storm like wave conditions.

Each model kelp frond is discretized into 50 nodes, and initially starts at rest in a vertically upright position. To maximize accuracy while preserving stability, we set a time step of $\Delta t = T_p/10000$. We found that generally, the model kelp fronds required 5-7 wave periods before reaching an equilibrium cycle. Thus, we ran each simulation for 10 wave cycles, and only data from the last wave cycle were utilized for analysis. Tests showed no sensitivity of the results to using more nodes or reducing the time step.

It is rather difficult to perform validation of our code, as most detailed data from flume experiments available (e.g. Zeller et al., 2014; Luhar & Nepf, 2016) is for systems in which the bending stiffness is important. Therefore, we validate the model and test the assumption that stiffness is not important against the theory for steady flow developed by Luhar and Nepf (2011), and present results for the range of kelp and wave properties relevant to our study in Appendix A.

2.3 Theory

Luhar and Nepf (2016) first introduced three dimensionless parameters that govern blade motion in wave conditions: the Cauchy number (Ca), buoyancy parameter (B), and the ratio of blade length to wave excursion (L). These parameters are given by

$$Ca = \frac{\frac{1}{2}\rho_w C_d A U_w^2}{\frac{EI}{l^2}} \tag{9}$$

$$B = \frac{(\rho_w - \rho_k) g V}{\frac{EI}{l^2}} \tag{10}$$

$$L = \frac{l\omega}{U_w} = \frac{l}{\Delta x_w} \tag{11}$$

Note that quantities denoted without the subscript i refer to the same variable for the entire frond instead of per segment (e.g., A_i is the projected frond area for each segment in the numerical model, while A is the projected area for the entire frond).

The Cauchy number Ca represents the ratio of drag forces (the most common force driving plant motion) to restoring force due to stiffness, while B represents the ratio of buoyancy to stiffness (i.e., the two forces that act to reduce plant motion). The parameter L also impacts blade dynamics, as is discussed below. Here, I is the second moment of area (for kelp stipes with circular cross-sectional area, $I = \pi r_s^4/4$, where r_s is the radius of the stipe), and U_w and Δx_w are characteristic scales for the horizontal wave orbital velocities and excursions, respectively. Because kelp fronds are typically much longer and grow in deeper water than seagrasses, the variation of the wave orbital velocity along the length of the frond can be important. We define U_w as the amplitude of the horizontal wave orbital velocity averaged over the length of the frond

$$U_w = \frac{1}{l}\int_0^l A_w \omega \frac{\cosh(kz)}{\sinh(kH)} dz = \frac{A_w \omega}{kl} \frac{\sinh(kl)}{\sinh(kH)}. \tag{12}$$

Consequently, we also define Δx_w as an average along the length, or $\Delta x_w = U_w/\omega$. In this way, L is interpreted as the ratio between frond length and average horizontal wave excursion. Note that as a result of our definition of U_w, any parameter that is function of U_w implicitly takes into account the impact of wave decay with depth.

In most seagrasses, drag is the main force driving motion, bending stiffness is the main restoring mechanism, buoyancy in negligible, and blade dynamics and drag reduction can be fully characterized by Ca and L. In steady flow, for $Ca \ll 1$, the blade remains upright and has very little drag reduction (Luhar & Nepf, 2011). For $Ca \gg 1$, significant bending occurs before the restoring force balances the drag force and this reconfiguration allows for a large drag reduction (via reduction in the plant surface area). In unsteady flows, drag reduction in the $Ca \gg 1$ limit also depends on the excursion of the blade, which Luhar and Nepf (2016) quantified using L. When $L \ll 1$, the blade length is much smaller than the wave excursion, so the blade should reach a maximum excursion while the fluid continues traveling past it. Thus, the blade behaves similarly as in steady flows, and drag reduction in this limit is still only dependent on Ca. On the other hand, when $L \gg 1$, the blade length is much larger than the wave excursion, so we expect that only the tip moves with the wave orbital velocity. The majority of the plant is akin to a rigid blade, and drag reduction is proportional to the product CaL.

Unlike seagrasses, kelp rigidity is very low (the stipe is very flexible), while buoyancy is very high. Therefore, drag forces are primarily balanced by buoyancy. As a result, for most wave conditions, stiffness plays an insignificant role in kelp motion (i.e, $Ca \gg 1$ and $B \gg 1$). Thus, for our cases, the buoyancy parameter

$$P = \frac{\frac{1}{2}\rho_w C_d A U_w^2}{(\rho_w - \rho_k) g V} = \frac{Ca}{B}, \tag{13}$$

first introduced by Nikora et al. (1998) is more relevant. Note that P is equivalent to Ca, except it measures the magnitude of the drag force in comparison to the resistance to bending provided by buoyancy. This definition is consistent with Henderson (2019), which built on previous results to develop a framework for the analysis of the response of aquatic vegetation to wave forcing in the presence of both buoyancy and stiffness. In particular, they identified the joint importance of CaL and PL in governing plant motion and drag reduction.

All of the studies discussed above start from the assumption that the Keulegan-Carpenter number is large and that the drag force is the main driver of blade motion. As we will show later, in many of our simulations, inertial forces are larger than the drag forces. To characterize this effect, we define the Keulegan-Carpenter number as

$$KC = \frac{\frac{1}{2}\rho_w C_d U_w^2}{\rho_w d(1 + C_a) U_w \omega} = \frac{C_d}{2(1 + C_a)} \frac{U_w}{\omega d}, \tag{14}$$

where d is a thickness associated with the cross sectional area ($d = V/A$). This specific definition, instead of the more traditional $KC = 2\pi U_w/(\omega d)$, is motivated by the scale analysis of the equations of frond motion and will be further discussed in Sec. 2.3.1.

For the wave and kelp conditions studied here, the values of B lie in the range of $O(10^3) < B < O(10^6)$, indicating that buoyancy forces are the dominant restoring forces preventing mo-

Table 2. List of numerical simulations and their associated dimensionless parameters defined in Equations (13), (11), and (14). Wave periods of 5 s, 10 s, 15 s, 20 s correspond with wave numbers of 0.167 m^{-1}, 0.063 m^{-1}, 0.04 m^{-1}, 0.03 m^{-1}, respectively.

H_s [m]	T_p [s]	l = 2 [m]			l = 5 [m]			l = 10 [m]		
		P	L	KC	P	L	KC	P	L	KC
0.25	5	0.0094	57.2	0.071	0.011	130.0	0.078	0.021	189.9	0.11
0.25	10	0.044	13.3	0.31	0.045	32.7	0.31	0.050	62.2	0.33
0.25	15	0.054	8.0	0.51	0.054	19.8	0.51	0.056	38.8	0.52
0.25	20	0.055	5.9	0.69	0.056	14.7	0.69	0.057	29.0	0.70
0.5	5	0.038	28.6	0.14	0.045	65.0	0.16	0.085	95.0	0.21
0.5	10	0.18	6.6	0.61	0.18	16.3	0.62	0.20	31.1	0.65
0.5	15	0.22	4.0	1.02	0.22	9.9	1.03	0.23	19.4	1.05
0.5	20	0.22	2.9	1.38	0.22	7.3	1.40	0.23	14.5	1.40
1	5	0.15	14.3	0.28	0.18	32.5	0.31	0.34	47.5	0.43
1	10	0.70	3.3	1.23	0.72	8.2	1.24	0.79	15.6	1.31
1	15	0.86	2.0	2.04	0.87	5.0	2.05	0.90	9.7	2.09
1	20	0.89	1.5	2.76	0.89	3.7	2.77	0.91	7.2	2.80
2	5	0.60	7.2	0.57	0.73	16.3	0.63	1.36	23.7	0.86
2	10	2.80	1.7	2.45	2.88	4.1	2.49	3.17	7.8	2.61
2	15	3.43	1.0	4.08	3.47	2.5	4.1	3.61	4.9	4.18
2	20	3.55	0.74	5.53	3.57	1.8	5.54	3.65	3.6	5.61

tion and that bending stiffness can be safely neglected (see also discussion in the appendix). The corresponding values of the Cauchy number are $O(10) < Ca < O(10^6)$. Thus, the relevant parameters characterizing our simulations are P, L, and KC, and values are listed on Table 2.

2.3.1 Scaling

To gain some insight into frond behavior, we follow the approach used by Henderson (2019) and start from a horizontal force balance of the governing equation of frond motion, Eq. (7). Here, we write the equation for the entire kelp frond, as opposed to the discrete version we use in the numerical model. In particular, Henderson (2019) assumes an equilibrium (i.e., a force balance with no frond acceleration) and neglects the vertical velocities. Instead, we keep the horizontal acceleration term and write Eq. (7) as

$$\begin{cases} (\rho_k + C_a\rho_w)\dfrac{du_k}{dt} = \dfrac{1}{2}\rho_w C_d \dfrac{A}{V}|u_x - u_k|(u_x - u_k) + (\rho_w + C_a\rho_w)\dfrac{\partial u_x}{\partial t} + \dfrac{EA_c}{V}\left(\dfrac{|\mathbf{x}| - l}{l}\right)\sin\theta \\ -(\rho_k - \rho_w)g + \dfrac{EA_c}{V}\left(\dfrac{|\mathbf{x}| - l}{l}\right)\cos\theta = 0 \end{cases} \tag{15}$$

Here, θ is the angle of deflection from the vertical, u_x is the representative horizontal wave velocity at the frond tip, u_k is the horizontal component of the tip velocity of the kelp $d\mathbf{x}/dt$, and $\mathbf{x}$ is the position of the frond tip. We proceed by assuming that θ is small enough so that the small angle approximation $\cos\theta \approx 1$ can be invoked, reducing the vertical balance in (15) to

$$(\rho_k - \rho_w)g = \frac{EA_c}{V}\left(\frac{|\mathbf{x}| - l}{l}\right) \tag{16}$$

which yields the new horizontal balance

$$(\rho_k + C_a\rho_w)\frac{du_k}{dt} = \frac{1}{2}\rho_w C_d d|u_x - u_k|(u_x - u_k) + (\rho_w + C_a\rho_w)\frac{\partial u_x}{\partial t} + (\rho_k - \rho_w)g\frac{x}{l} \tag{17}$$

Note that we also used $\sin\theta = x/l$.

Normalizing by ρ_w, U_w, ω, and Δx_w, Eq. (17) can be written as

$$\frac{PL}{KC}\left[\frac{du_k^*}{dt^*} - \frac{\partial u_x^*}{\partial t^*}\right] = PL\left[|u_x^* - u_k^*|(u_x^* - u_k^*)\right] + [x^*]\,, \tag{18}$$

where we used the approximation $\frac{(\rho_k/\rho_w + C_a)}{(1+C_a)} \approx 1$. Here, all the terms denoted by * are dimensionless and assumed to be of order unity.

The equivalent equation for the force balance (i.e., assuming no acceleration) as done in Henderson (2019) is given by

$$\frac{PL}{KC}\left[-\frac{\partial u_x^*}{\partial t^*}\right] = PL\left[|u_x^* - u_k^*|(u_x^* - u_k^*)\right] + [x^*]\,. \tag{19}$$

The more complete Eq. (18) and its force balance version (19) both suggest the use of PL and PL/KC as two main scaling parameters. A visualization of this two-dimensional parameter space is given in Fig. 3.

It is useful to understand the behavior of kelp fronds in three asymptotic regimes: (1) the "buoyancy dominated" regime, given by $PL \ll 1$ and $PL/KC \ll 1$ and corresponding to points in the red region and closer to the origin in Fig. 3(a), (2) the "drag dominated" regime, given by $PL \gg 1$ and $KC \gg 1$ and corresponding to points in the blue region and closer to the bottom right corner of Fig. 3(a), and (3) the "inertia dominated" regime, given by $PL/KC \gg 1$ and $KC \ll 1$ and corresponding to points in the yellow region and closer to the top left corner of Fig. 3(a).

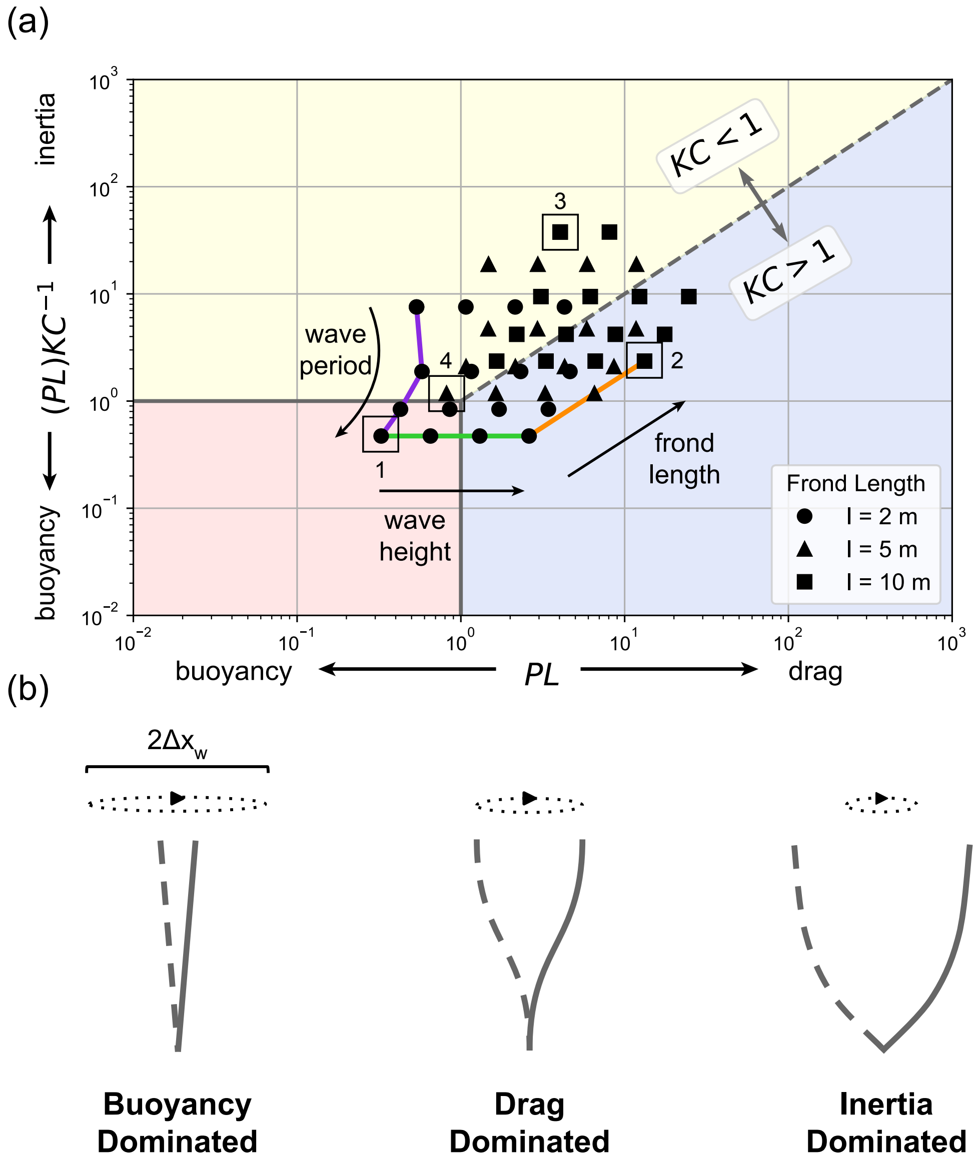

Figure 3. (a) The parameter space for kelp motion. The red region represents where motion is buoyancy dominated; blue represents where motion is drag dominated; yellow represents where motion is inertia dominated. The gray lines represent the dividers $PL = 1$, $PL/KC = 1$, and the dashed gray line is $KC = 1$. The black points are where our simulations fall, where different shapes represent each of the plant lengths. The purple, green, and orange solid lines show increasing wave period, wave height, and plant length, respectively. Black squares 1, 2, 3, and 4 denote cases selected for further analysis in later sections. (b) Expected kelp motion in each asymptotic regime.

In the "buoyancy dominated" regime, Eq. (18) suggests $x^* \ll 1$, which implies $x \ll \Delta x_w$ (i.e., Δx_w is not the appropriate scale for the horizontal excursion of the tip). Here, buoyancy is very strong and severely limits plant motion as depicted in Fig. 3(b). This is equivalent to the nearly rigid plant configuration considered by both Luhar and Nepf (2016) and Henderson (2019).

The "drag dominated" regime corresponds to the small excursion limit of Luhar and Nepf (2016) and Henderson (2019). Here, drag forces are much larger than inertial forces and the frond motion is driven mostly by drag. In this case, the left hand side of Eq. (18) is approximately 0, resulting in the following simplification:

$$|u_x^* - u_k^*|(u_x^* - u_k^*) = \frac{|x^*|}{PL}. \tag{20}$$

Since $PL \gg 1$, it is expected that cases in this regime should have small relative velocity, or that $|u_x^* - u_k^*|(u_x^* - u_k^*) \ll 1$. The frond should move closely with the wave motion, meaning that $x^* \approx 1$, or $x \approx \Delta x_w$ as illustrated in Fig. 3(b).

Finally, in the "inertia limit", inertial forces are much larger than drag and buoyancy. Thus, we can assume that

$$\frac{PL}{KC}\left[\frac{du_k^*}{dt^*} - \frac{\partial u^*}{\partial t^*}\right] \gg PL\left[|u_x^* - u_k^*|(u_x^* - u_k^*)\right], \tag{21}$$

and applying that simplification to Eq. (18) yields

$$\frac{PL}{KC}\left[\frac{du_k^*}{dt^*} - \frac{\partial u^*}{\partial t^*}\right] = [x^*]\,. \tag{22}$$

Because $PL/KC \gg 1$, this requires

$$\left[\frac{du_k^*}{dt^*} - \frac{\partial u_x^*}{\partial t^*}\right] \propto \left(\frac{PL}{KC}\right)^{-1}, \tag{23}$$

implying that the two accelerations are of the same order of magnitude. In practice, this means that the frond acceleration is mostly caused by the same pressure gradient force that is driving the wave motion. Because kelp is less dense than the fluid ($\rho_k < \rho_w$), the frond acceleration in response to the same pressure gradient force is larger than that of a fluid parcel, causing the frond to perform an orbital motion with larger horizontal displacements than the fluid itself. Hence, when $PL/KC \gg 1$, we also have $x^* = x/\Delta x_w > 1$, meaning that it is possible for the kelp excursion to be greater than the wave excursion.

2.3.2 Drag Coefficient Scaling

The varying flexibility of aquatic vegetation can reduce the drag force exerted on the flow by two mechanisms: (1) a reduction of the frontal area exposed to the flow, and (2) a reduction in the relative velocity due to synchronous motion of vegetation and water. Luhar and Nepf (2011) quantified this effect by defining the effective length, l_e, which represents the length of a rigid blade that generates the same drag as a flexible blade of length l. Physically, l_e/l represents the ratio of the real horizontal drag force (F_D) to the horizontal drag force experienced by a rigid blade ($F_{D,Rig}$). Alternatively, it is equivalent and sometimes more convenient to define a reduced drag coefficient $C_{d,f}$ to represent the effect of motion on the drag force (Razmi et al., 2020), or

$$\frac{l_e}{l} = \frac{F_D}{F_{D,Rig}} = \frac{C_{d,f}}{C_d}. \tag{24}$$

If $C_{d,f}$ is known, one can calculate the true drag force using the fluid velocity (without explicit knowledge of the vegetation motion) via

$$F_D = \frac{1}{2}\rho_w C_{d,f} A|u_x|u_x. \tag{25}$$

The drag reduction due to plant motion is modeled by the reduced value of $C_{d,f}$ (when compared to C_d).

Luhar and Nepf (2016) found that for plants where the restoring force is primarily from the bending rigidity, $C_{d,f}/C_d \propto (CaL)^{-1}$. Henderson (2019) considered the case with both bending rigidity and buoyancy when the motion is driven by a linearized drag force. Their solution recovers the result from Luhar and Nepf (2016) when buoyancy in negligible and yields a new result for the case of interest here, where buoyancy is the dominant restoring mechanism. In this case, their result yields

$$\frac{C_{d,f}}{C_d} = \left[\frac{\pi^2/(4PL)^2}{1+\pi^2/(4PL)^2}\right]^{1/4}, \tag{26}$$

which transitions from a region in which $C_{d,f}/C_d \approx 1$ in the buoyancy dominated regime to $C_{d,f}/C_d \propto (PL)^{-1/2}$ for large PL in the drag dominated regime. Previous studies did not consider the cases where inertia is important ($KC \ll 1$), and it is unclear how that would impact the total drag force.

2.3.3 Parameter Space

The cases shown in Table 2 are presented on the parameter space formed by PL and PL/KC in Fig. 3. For most wave conditions, our simulations are in a transition region ($KC \approx 1$, $PL \approx 1$, or $PL/KC \approx 1$), so we do not expect to observe results that resemble the asymptotic conditions discussed in Section 2.3.1. Note that most studies to date have focused on the regime in which $KC \gg 1$, investigating motion and drag in the transition between the red and blue regions.

To facilitate interpretation of our results presented in the next sections, we have included in Fig. 3 arrows indicating how varying wave properties and frond length impact the location of points on the parameter space. Wave orbital velocity amplitudes are proportionate to $A_w\omega$, so larger wave periods (and smaller wavenumbers) generally leads to smaller PL and larger KC values. In other words, increasing wave period (reducing wavelength) results in cases where buoyancy is relatively larger and drag is more important than inertial forces. Lines of increasing wave height have constant PL/KC values (parallel to the x-axis in Fig. 3), transitioning further away from the limiting behavior of buoyancy or inertia dominated regimes into the drag dominated regime. Similarly, only increasing frond length does not affect KC, but correlates with increasing PL and PL/KC values, meaning buoyancy becomes relatively less important.

3 Results and Discussion

3.1 Characterization of Kelp Motion

In general, model kelp responded to different wave conditions with a wide range of behavior. Initially, all upright fronds undergo an adjustment period that lasts a few wave periods before they reach an equilibrium cycle, the type of which depends on where the simulation falls in the parameter space of Fig. 3(a).

Fig. 4 shows example frond excursion plots for different regimes of kelp motion: buoyancy dominated, drag dominated, inertia dominated, and a transition case (refer back to Figure 3(a) for where each case is located in the parameter space). Animations for these four cases are presented in the Supporting Information. For each case, we also show how the relative horizontal frond excursion

$$\delta x = \frac{(x_{\max} - x_{\min})}{2\delta x_w(\bar{z})} \tag{27}$$

varies along the length of the plant. Here, $2\delta x_w(\bar{z})$ is the local horizontal wave excursion at the mean vertical position of each segment over the wave cycle, or

$$\delta x_w(\bar{z}) = A_w\omega \cosh(k\bar{z})/\sinh(kH) \tag{28}$$

Physically, δx is a measure of the frond excursion normalized by the average wave excursion.

In the buoyancy dominated region of the parameter space (Case 1, Fig. 4a), the frond excursion is less than the wave excursion as the entire frond remains mostly upright. The maximum frond excursion is <90% of the horizontal wave excursion. In this case, $PL \approx 0.3$ and $(PL)/KC \approx 0.5$, so buoyancy is only around 2-3 times larger than the other forces, which is why the blade ex-

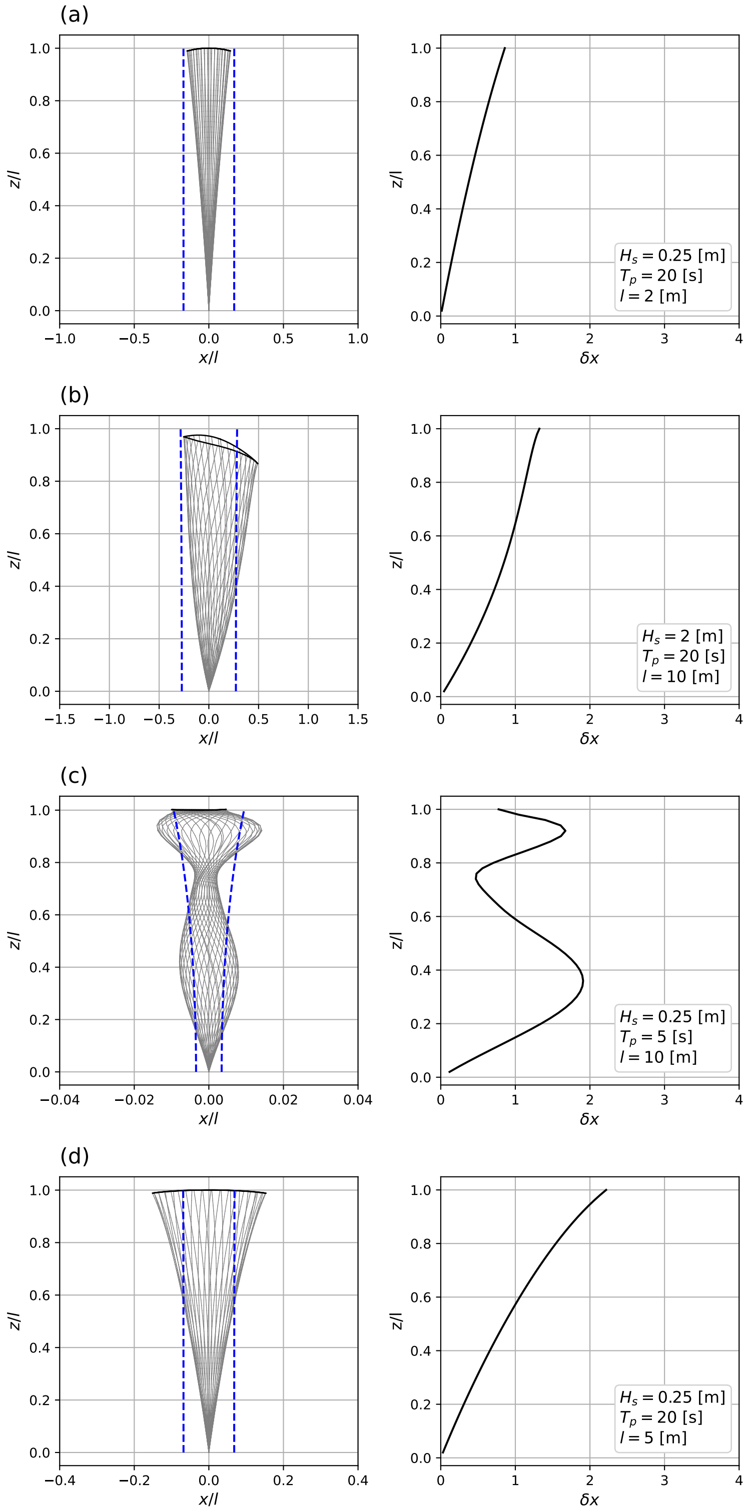

Figure 4. The cases of kelp motion from different regions of the parameter space; see Figure 3(a). Left panels are blade excursions over one equilibrium wave cycle; blue dashed lines represent the horizontal wave excursion at each depth. Both axes are normalized by plant length (l). Right panels are relative horizontal excursion plots for the buoyancy dominated case. (a) Case 1: buoyancy dominated. (b) Case 2: drag dominated. (c) Case 3: inertia dominated. (d) Case 4: transition.

cursion is still fairly large. As points move farther into the buoyancy dominated regime (closer to the origin in the parameter space), we expect that the maximum blade excursion would decrease to nearly zero.

For drag dominated cases (Case 2, Fig. 4b), the upper half of the frond moves more-or-less with the wave, while the bottom portion of the frond moves less than the wave excursion around it. A slight concavity in the profile of δx indicates that the majority of drag is being generated in the bottom 50% of the frond, as postulated by Henderson (2019). There is a part of the tip that moves about 30% more than the wave, which we hypothesize may be the additional effects of the inertial forces or asymmetric motion. Overall, this is the classic example of drag reduction in flexible vegetation due to synchronous oscillation with the wave motion (i.e., reduction in relative velocity between the frond and the water).

In the inertia dominated limit (Case 3, Fig. 4c), a majority of the frond (around 60%) moves more than the wave excursion. Note that the displacements are only a small fraction of the plant length, and that the aspect ratio of the figure is highly distorted. The maximum frond excursion is almost twice as large as the wave excursion; this is clearly a much greater effect than in the previous two cases. Different portions of the frond are out of phase with each other (the animation included in Supporting Information is particularly illuminating here), corresponding to a higher natural mode of vibration. This would be equivalent to mode 2 motion identified by Mullarney and Henderson (2010). This higher mode leads to a non-monotonic variation of the amplitude of the frond motion along its length, and we hypothesize that higher inertial forces potentially lead to the amplification of higher natural modes of motion.

Finally, we included a typical example of our transition cases (Case 4, Fig. 4d). Here, the frond excursion plots displays a mix of traits from the other three limits. About half of the frond moves more than the wave, with the tip moving over twice as much as the fluid does. The frond also stays relatively upright and straight, as in the buoyancy dominated regime. Unlike the inertia dominated example, there is a smooth transition in the amplitude of kelp motion.

Despite the large variation in frond motion depending on the dominant forcing mechanisms, some general conclusions are possible. For a fixed frond length l, the relative horizontal blade excursion δx decreases with increasing KC. When $KC < 1$ (inertial forces are larger than drag forces), the entire frond moves more than the wave excursion. On the other hand, when $KC > 1$, a majority of the frond moves less than the wave, with the tip moving about the same. Figure 5 illustrates how the average of δx over the frond length, denoted $\overline{\delta x}$, varies with KC. Clearly,

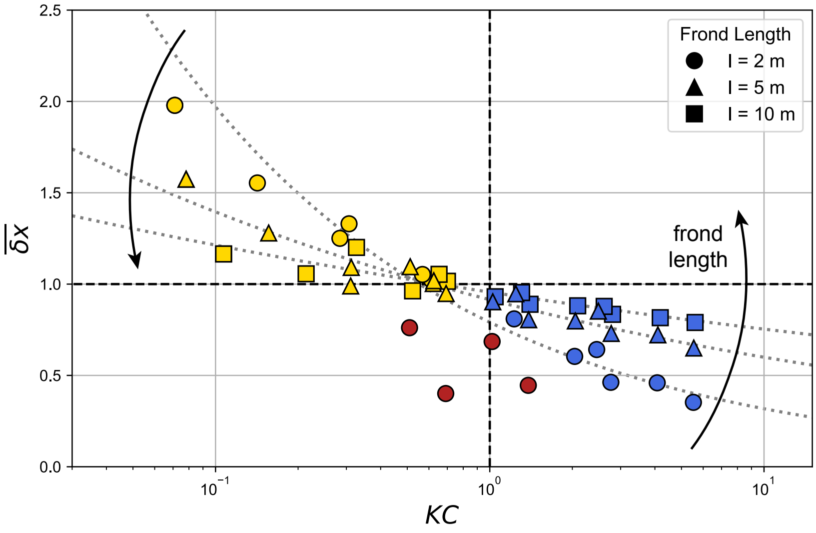

Figure 5. Variation in relative horizontal excursion, averaged over length of the blade ($\overline{\delta x}$) with KC. Yellow points are inertia dominated ($PL/KC > 1$ and $KC < 1$), red are buoyancy dominated ($PL < 1$ and $PL/KC < 1$), and blue are drag dominated ($PL > 1$ and $KC > 1$). Different shapes represent different frond lengths, with circles representing 2 m fronds, triangles are 5 m, and squares are 10 m. Dashed lines were added to facilitate interpretation.

for each frond length, $\overline{\delta x}$ reduces with increasing KC. The buoyancy dominated cases (red symbols) appear as outliers, having much smaller excursions than suggested by the behavior of neighboring points.

Luhar and Nepf (2016) described the relative blade excursion for seagrasses (bending resistance being the dominant restoring force) in the large KC (drag dominated) regime. In particular, they argued that $\overline{\delta x} \approx 1$ for $L \gg 1$ and $\overline{\delta x} \ll 1$ for $L \ll 1$. Note that in our cases, Eqs. (11) and (14) imply $L \propto (l/d)KC^{-1}$. Since we keep the stipe diameter d constant in all our simulations, at a constant value of KC we have $L \propto l$. Results in Fig. 5 agree with Luhar and Nepf (2016) for the large KC regime ($KC > 1$, represented by blue symbols), in that at a fixed value of KC, $\overline{\delta x}$ increases with increasing L and approaches $\overline{\delta x} \approx 1$ for large L. Interestingly, all the frond lengths seem to match the wave excursion for $KC \approx 0.7$, and the behavior switches for values of KC below this threshold (i.e., in the inertia dominated regime) where fronds have larger excursions than the water and $\overline{\delta x}$ increases with decreasing L. In this small KC regime, $\overline{\delta x} \approx 1$ still holds for large L, but $\overline{\delta x} \gg 1$ for $L \ll 1$. Therefore, the unifying conclusion from Fig. 5 valid across the entire KC regime is that $\overline{\delta x} \approx 1$ for $L \gg 1$, and deviations increase with increasing L in different directions depending on the dominant forcing mechanism (drag vs. inertia).

3.2 Characterization of Drag Forces

In our numerical simulations, the drag force is a function of position along the frond and time. We follow Luhar and Nepf (2016) and integrate the horizontal drag force over the frond length, and take its root mean square (RMS) value over one wave cycle to characterize the total drag for each simulation. We verified that as tested by Luhar and Nepf (2016), using the maximum value over the cycle here as well does not produce significant changes. Therefore, we calculate the drag reduction as

$$\frac{C_{d,f}}{C_d} = \frac{[F_D]_{RMS}}{\left[F_{D,Rig}\right]_{RMS}} = \frac{\left[\int_0^l \frac{1}{2}\rho_w C_d a|\mathbf{u} - \frac{d\mathbf{x}}{dt}|(u_x - \frac{dx}{dt})dl\right]_{RMS}}{\left[\int_0^l \frac{1}{2}\rho_w C_d a|\mathbf{u}|u_x dz\right]_{RMS}}, \tag{29}$$

where $a = A/l$ is the maximal frond projected area per unit length (i.e., the frond area density).

Resulting values of $C_{d,f}/C_d$ are displayed as a function of PL and separated by drag dominated ($KC \leq 1$) and inertia dominated ($KC > 1$) regimes in Fig. 6a. As expected, there is good agreement between our drag-dominated cases ($KC > 1$, circles) and the prediction from Henderson (2019) given by Eq. 26. Our own power-law fit to these cases yields

$$C_{d,f}/C_d = (PL)^{-0.6} \tag{30}$$

across the entire range of PL, extending to values larger than 1 for $PL < 1$ (to be discussed below). The small difference in exponent likely originates, among other things, from the linearized drag approximation employed in the derivation of (26) and the presence of inertial forces in our simulations.

On the other hand, the inertia dominated cases ($KC < 1$, triangles) do not scale as well with Eq. (26). Generally, values of $C_{d,f}/C_d$ seem to be independent of KC in the range $PL < 1$, but the power-law decay in the large PL region is steeper for the inertia dominated cases. We expect the drag reduction to be a joint function of PL and KC, but unfortunately our simulated cases are not enough to support a two-dimensional fit with any confidence. Instead, we note that both Eq. (26) and the empirical fit (30) can serve as an upper bound on the true drag. Our best fit for the inertia dominated cases yields $C_{d,f}/C_d = 0.7(PL)^{-0.8}$.

Two important features of Fig. 6 require further explanation: the larger drag reduction in the inertia dominated cases and the increase in drag compared to a rigid frond (i.e. drag augmen-

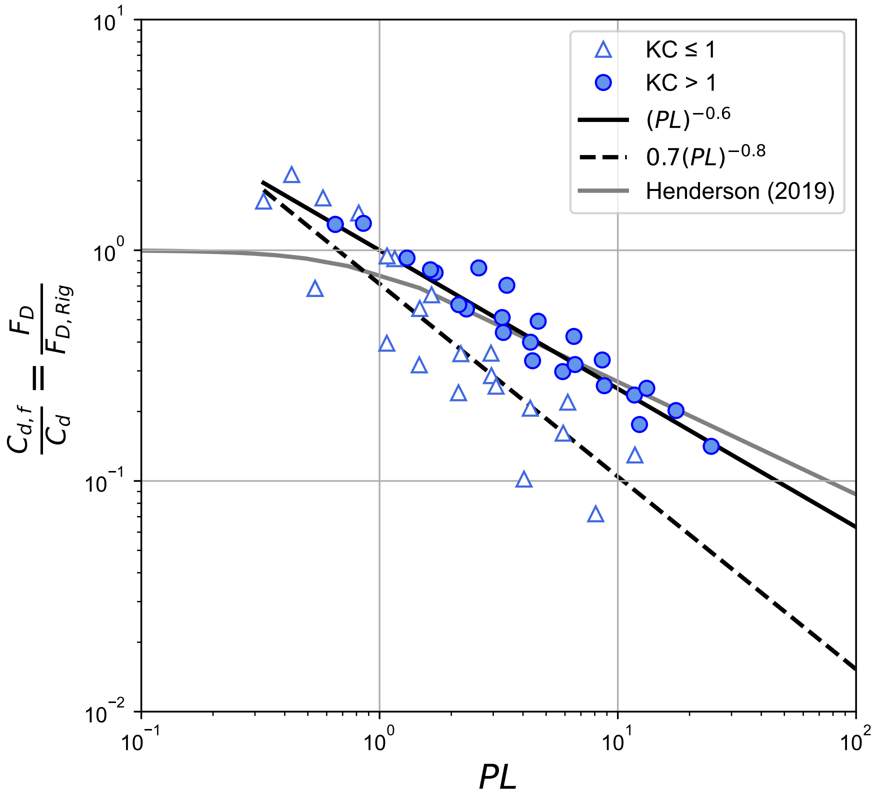

Figure 6. Effective drag coefficients calculated using horizontal drag force only versus PL. The solid black line is the best fit ($R^2 = 0.92$) for cases where $KC > 1$, while the dashed black line is the best fit ($R^2 = 0.86$) for $KC < 1$. The gray line represents Eq. (26). Triangles represent cases where $KC < 1$, while circles are cases where $KC > 1$.

tation) for most cases in which $PL < 1$. To address these questions, we note once again that in our model all changes to drag are caused by the relative velocity between the frond and the water. We define a normalized relative velocity

$$u_{rel} = \frac{(u_x - dx/dt)}{U_w}, \tag{31}$$

and show the variation of u_{rel} over one equilibrium wave period at several locations along the frond in Fig. 7 for the four sample cases illustrated in Fig. 4 (refer to Fig. 8b for the specific $C_{d,f}/C_d$ value corresponding to the cases shown in Fig. 7).

In a typical drag dominated case, the upper portion of the frond moves with the waves, reducing the relative velocities towards the frond tip (e.g., see Figure S1 of the Supporting Information). In this case, most of the drag originates from the bottom of the frond where the relative velocities are comparable to the wave velocity due to restricted frond motion (Luhar & Nepf, 2016; Henderson, 2019). In our selected drag dominated case (Fig. 7b), the behavior is already more complex than that. The relative velocity at a given time switches sign between the bottom and the top of the frond (e.g., at $t/T_p = 0.5$ we have $u_{rel} > 0$ at $z/l = 0.2$ and $u_{rel} < 0$ at $z/l = 1.0$). This change in sign occurs when the frond velocity in the upper portion of the frond is larger than the wave velocity, which happens when the frond excursion is larger than that of the fluid as described in the previous subsection (see Fig. 4b). The cancellation between drag forces from the top and bottom of the frond lead to additional drag reduction in comparison to the typical case described above, and it may also in part explain the steeper $(PL)^{-0.6}$ decay of $C_{d,f}/C_d$ in comparison to the prediction by Henderson (2019).

In order to explain the drag augmentation that occurs for most cases with $PL < 1$, we contrast the classic drag reduction behavior to that observed for the buoyancy dominated case in Fig. 7a (which has $C_{d,f}/C_d \approx 1.6$, as seen in Fig. 8b). Here we notice that, contrary to expectations, the relative velocity (and therefore the drag force) monotonically increases from the bottom to the top of the frond. This is only possible if the frond velocity is out-of-phase with the water velocity so that $(u_x - dx/dt) > u_x$ (e.g., when $u_x > 0$, we must have $dx/dt < 0$ for this to be possible). In this case, most of the drag actually comes from the tip of the frond, and the total drag is larger than that of a rigid frond, yielding $C_{d,f}/C_d > 1$. Therefore, we conclude that drag augmentation is a physical feature of flexible vegetation that occurs when the frond motion is out-of-phase with the wave orbital velocity and it must also be taken into account. This out-of-phase motion is caused by inertial forces (note that the pressure gradient force is 90 degrees out of phase with the wave motion).

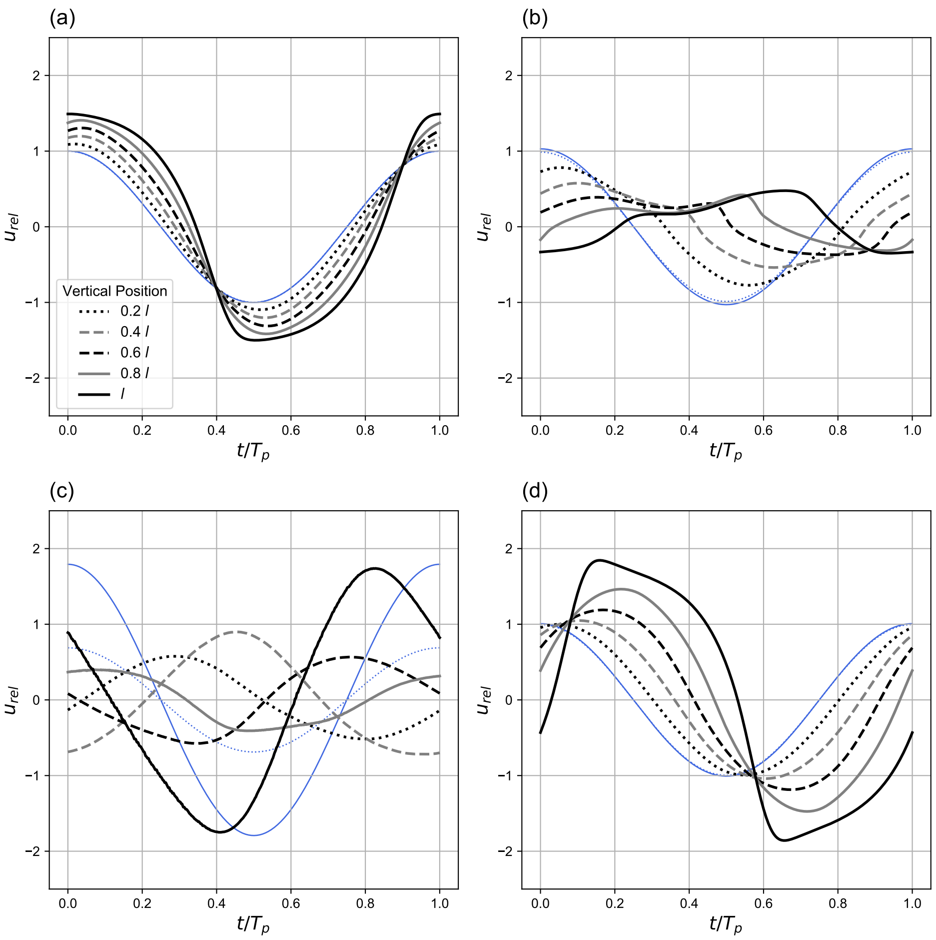

Figure 7. Relative velocities at five different locations along the length of the blade (0.2 l, 0.4 l, 0.6 l, 0.8 l, and l) over the course of one wave cycle for each case of frond motion. Solid and dotted blue lines indicate the fluid velocity at the tip of the frond and at 0.2l, respectively. All velocities are normalized by U_w. (a) Case 1: buoyancy dominated, H_s = 0.25 [m], T_p = 20 [s], l = 5 [m]. (b) Case 2: drag dominated, H_s = 2 [m], T_p = 20 [s], l = 10 [m]. (c) Case 3: inertia dominated, H_s = 0.25 [m], T_p = 5 [s], l = 10 [m]. (d) Case 4: transition, H_s = 0.25 [m], T_p = 20 [s], l = 5 [m].

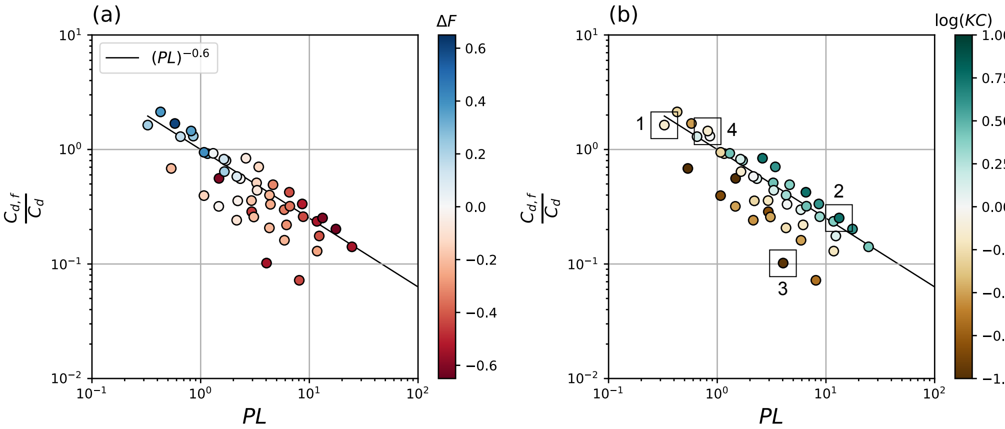

Figure 8. (a) $C_{d,f}/C_d$ versus PL, where points are colored by $\log(KC)$. Positive color values indicate $KC > 1$, while negative values represent points with $KC < 1$. (b) $C_{d,f}/C_d$ versus PL, where points are colored by $\Delta F_{D,l}$, which quantifies the difference between the drag exerted by the bottom half of the plant and the top half. Black squares 1, 2, 3, and 4 represent the same cases referenced in 3a. In both panels, the black line is the same best fit as in Fig. 6.

To further characterize this behavior, we define the parameter

$$\Delta F = \frac{[F_{D,top}]_{RMS} - [F_{D,bot}]_{RMS}}{[F_{D,top}]_{RMS} + [F_{D,bot}]_{RMS}} \tag{32}$$

where $[F_{D,top}]_{RMS}$ and $[F_{D,bot}]_{RMS}$ are the RMS of the drag integrated over the top half and bottom half of the frond. When ΔF is positive, more drag is generated by the top half of the frond than the bottom half; the opposite is true when ΔF is negative. Figure 8a shows $C_{d,f}/C_d$ against PL, but with points colored by ΔF. All the points with $C_{d,f}/C_d > 1$ have positive ΔF values, meaning that a majority of the drag is originated from the top half of the frond, thus implying out-of-phase motion between frond and water. In our most extreme case, the drag force from the upper half of the frond is almost four times as large as that of the bottom half. We have verified that all these cases with drag augmentation have relative velocity profiles similar to the one shown in Fig. 7a.

As previously discussed, the drag force decays even faster than $(PL)^{-0.6}$ in the inertia dominated cases. For the case illustrated in Fig. 7c, we see that the drag force changes sign twice between the bottom and the top of the frond. This is in part associated with the complex behavior associated with the higher natural mode that corresponds to the motion of these cases (see Fig. 4c). The large cancellations of the drag force along the frond in these cases with $KC < 1$ lead to much smaller values of the total drag in comparison to other cases. This is clearly seen in Fig.

8b, where $C_{d,f}/C_d$ is displayed against PL and colors represent their value of $\log KC$. Positive color values represent simulations where $KC > 1$, and negative color values represents simulations where $KC < 1$. There is generally a smooth decrease in KC as points move farther away from the best fit line for the large KC regime, suggesting a smooth reduction in $C_{d,f}/C_d$ with decreasing KC. As a result, this type of motion appears even more "flexible" than in the drag dominated regime. Note also that these inertia dominated cases tend to have more drag originating from the bottom of the frond or, at most, an even distribution between top and bottom drag (see Fig. 8a).

Finally, our transition case (Fig. 7d) displays a mix of traits from the three aforementioned cases, including increased drag from the upper portion of the frond due to out-of-phase motion with the water (and associated $C_{d,f}/C_d > 1$) and a switch in sign of the drag along the frond due to larger frond excursions in comparison to water parcels. For more elaboration on how to interpret Fig. 7, please refer to Figure S1 of the Supporting Information.

3.3 Asymmetric Motion

Another interesting aspect of flexible vegetation motion is the degree of asymmetry, even under symmetric wave forcing. Zhu et al. (2020) conducted an in depth analysis of the conditions for asymmetric blade motion, concluding that there are only a few conditions where blade motion is nearly symmetric: (1) when blade length is much smaller than the wavelength $\lambda = 2\pi/k$, (2) blade length is much smaller than the water depth, or (3) the water depth is much smaller than the wavelength. In our simulations, wavelengths vary between $\lambda = 37$ m and $\lambda = 210$ m, so the vast majority of our cases satisfy both (1) and (3) and we would expect symmetric frond motion. Zhu et al. (2020) quantified degree of asymmetry defining $\beta_{xT} = \overline{x}/|x_{\max}|$, where $\overline{x}$ is the average displacement over an equilibrium cycle and $|x_{\max}|$ is the maximum horizontal displacement (they also used an arbitrary threshold $\beta_{xT} < 0.05$ for nearly symmetric motion). Based on the values of $|\beta_{xT}|$ shown in Fig. 9, most of our simulations display asymmetric motion. A few of our cases with $KC \leq 1$ had negative β_{xT} values, meaning that $\overline{x}$ is slightly negative even though the wave propagates in the positive x direction. This is likely due to the effects of inertial forces being out of phase with drag. To include these points, we chose to plot the absolute value of β_{xT}.

Zhu et al. (2020) attributes the cause of asymmetric motion to be either the effect of vertical wave orbital velocities or spatial asymmetry of the encountered wave orbital velocities from

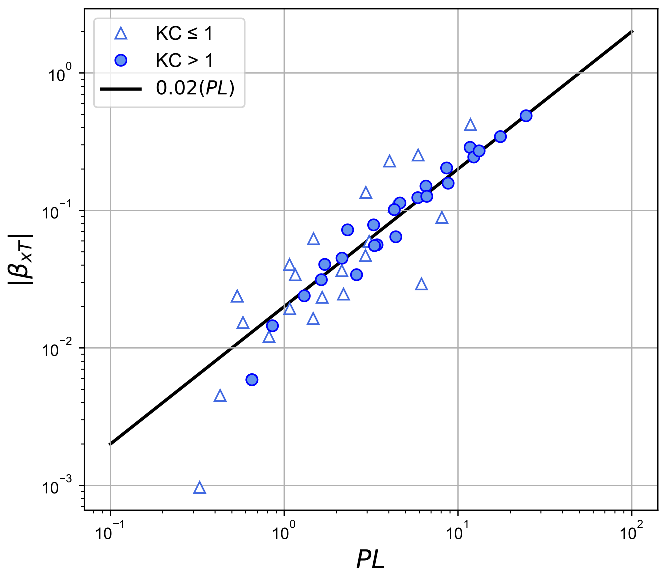

Figure 9. Degree of asymmetry, β_{xT} increases with PL. Blue filled circles are drag dominated cases ($KC > 1$); open triangles are inertia dominated ($KC \leq 1$). Black line represents the best fit for the $KC > 1$ points ($R^2 = 0.94$).

horizontal blade displacements. We performed numerical simulations removing these two effects (i.e., by setting the vertical wave velocity to zero and eliminating the forcing dependence on the x-position of the nodes) and observed only a very small reduction in the degree of asymmetry (not shown), suggesting that other mechanisms may be involved in our cases. Nevertheless, it is remarkable that the parameter PL is an excellent predictor of the degree of asymmetry measured by β_{xT}. The coefficient of determination (R^2) is larger than that for the drag coefficient reduction in Fig. 6, and even though the spread is larger for the inertia dominated cases, there seems to be no trend with KC as in the case of the drag coefficient. Note that increasing PL is mostly accomplished by increasing wave height, increasing frond length, or reducing buoyancy, conditions that are expected to lead to more asymmetric motion (Zhu et al., 2020). Importantly, the scaling of $C_{d,f}/C_d$ and β_{xT} with PL suggests that there is a correlation between drag reduction and motion asymmetry.

4 Conclusion

In this study, we developed a numerical model to investigate the motion of kelp fronds and its impact on drag forces in response to realistic monochromatic wave forcing. From the wave parameters retrieved from observations, it becomes clear that the usual assumption of weak inertial forces (i.e., large Keulegan-Carpenter number KC) is not always applicable to kelp motion in nearshore waters. A more detailed scaling analysis of the equations of frond motion suggests a 2-dimensional parameter space formed by a combination of KC, the buoyancy parameter P, and the ratio of frond length to wave horizontal excursion L. Motivated by the governing equation of motion, we chose to use PL and PL/KC as the two independent parameters. This leads to 3 asymptotic regimes (dominated by buoyancy, drag, and inertia) and successful classification of different types of frond motion (see Fig. 3).

We quantified the relative horizontal excursion of the frond in comparison to that of water, and the results shows strong dependence on KC and L. For the drag-dominated cases (large KC), frond excursion is smaller than water excursion, and differences increase with increasing KC and decreasing frond length. This is consistent with the analysis of Luhar and Nepf (2016). For the inertia dominated cases (small KC), frond excursion is larger than water excursion and differences increase with decreasing KC and frond length. Interesting, for all frond lengths, frond excursions match water excursion for $KC \approx 0.7$.

We have also investigated the extent that kelp motion impacts its drag reduction (in comparison to a rigid kelp frond). We quantify drag reduction by introducing a ratio of the true drag coefficient to that of a rigid frond $C_{d,f}/C_d$, and found that drag reduction is a function of KC and PL. Our empirical fit to simulation results yields

$$C_{d,f}/C_d = \begin{cases} (PL)^{-0.6} & \text{if } KC > 1 \\ 0.7(PL)^{-0.8} & \text{if } KC \leq 1 \end{cases} \tag{33}$$

The result for the drag dominated regime ($KC > 1$) is fairly close to the prediction by Henderson (2019). The steeper drag reduction with PL in the inertia dominated case ($KC \leq 1$) results from a reversal of the drag direction along the frond and cancellation between drag forces acting in opposite directions. We also observe drag augmentation (i.e., $C_{d,f}/C_d > 1$) for cases in which $PL < 1$, and track the origin of this to the motion of the frond being out-of-phase with the motion of the water.

It is important to note that drag reduction is directly associated with the efficiency of wave energy dissipation by the vegetation. As a general conclusion, in the regimes of frond motion studied here, the effective drag coefficient is reduced with increasing PL and decreasing KC. Waves with smaller periods correspond to smaller KC and larger PL, and thus smaller drag coefficient and less efficient energy dissipation. Similarly, increasing wave height increases PL (without affecting KC), leading to smaller drag.

Future research needs to extend the modeling to include effects of mean currents and broad-band wave spectra (and possibly turbulence) on the frond motion, and the presence of surface canopies. In addition, observational confirmation by synchronous measurements of wave and kelp motions are necessary to validate our modeling results.

Appendix A Model Validation

Due to lack of detailed observations of blade/frond motion and drag reduction for cases with negligible bending stiffness that could be used to validate our model assumptions, we test our model against the theory developed by Luhar and Nepf (2011) for bending of flexible blades in steady unidirectional flow. More specifically, we compare model results to the predictions of effective length given by their Equation 16, which includes both bending stiffness and buoyancy as restoring forces and can be written in terms of P as

$$\frac{l_e}{l} = 1 - \frac{1 - 0.9Ca^{-1/3}}{1 + 8Ca^{-3/2} + P^{-3/2}}. \tag{A1}$$

Note that this theory-based expression has empirical constants. We made small adjustments to our numerical model to better match the conditions used in Luhar and Nepf (2011). We modified the drag force to include the frontal area reduction due to blade bending (i.e., including the $\cos\theta$ term), and removed the drag force in the z direction (the relative velocity being defined only based on the x component).

Our goal is to test the hypothesis that, for our range of values of Ca and P, neglecting the bending stiffness (i.e., assuming $Ca \to \infty$) has a negligible effect on the results. Our study design uses all the kelp geometric and constitutive properties described in Section 2.2, neglecting the bending stiffness and still allowing for stretching of the blade. We tested model performance across a wide range of P by varying current velocity while holding buoyancy constant via kelp density. Results are shown in Fig. A1.

The effective length predicted by our model compares well to the results from Eq. (A1) across the entire range of P (Fig. A1a). The fractional error in predictions (Fig. A1b) is always below 10% for the range of P in our wave simulations ($0.01 < P < 4$). In addition to our neglect of bending stiffness, differences could also originate from the error between the simulations in Luhar and Nepf (2011) and their fitted equation, and also our inclusion of frond stretching. We note that

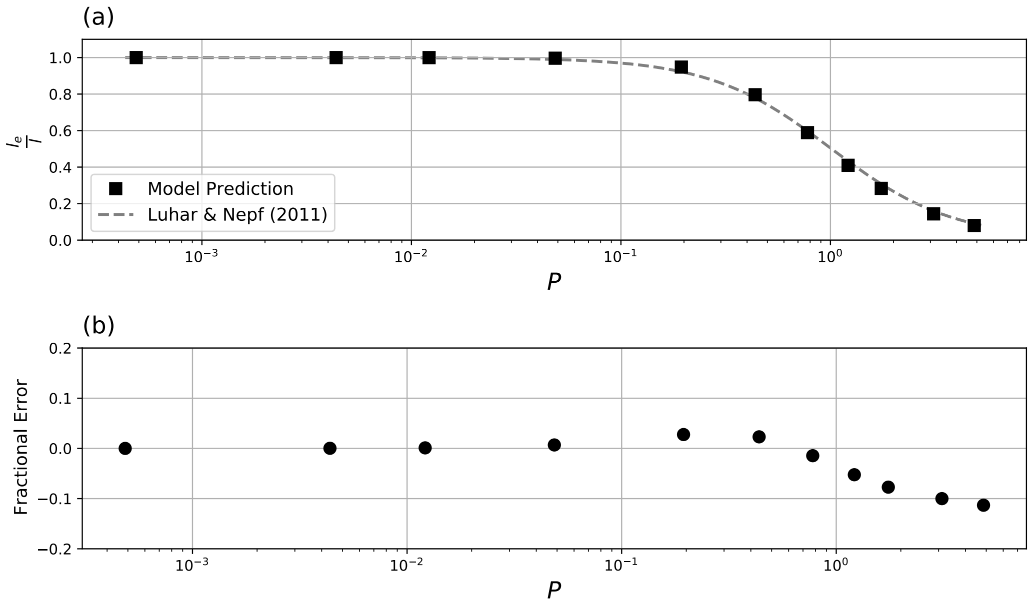

Figure A1. (a) Model predictions of effective length (black squares) compared to the model from Luhar and Nepf (2011) given by Eq. (A1) (dashed gray line). (b) Fractional error of present model predictions.

comparing Eq. (A1) including and neglecting Ca leads to errors of only up to 3% for the range of conditions used in our model. Therefore, despite the differences between blade response to a steady flow and our study of unsteady wave motion, we conclude that the errors incurred by neglecting bending stiffness in our numerical model are likely minor and would not impact the overall conclusions of our study.

Open Research Section

The data required to reproduce the figures will be made available at a public repository prior to final publication.

Acknowledgments

The authors report no conflict of interest.

This work is supported by the ARPA-E MARINER Program (DE-AR0000920). JFM also gratefully acknowledges support by the Sharon Fisher Endowment and the Norton Rodman Endowment (Undergraduate Research Scholars Program, UCLA Undergraduate Research Center – Sciences), and the Queen's Road Fellowship Program (with special thanks to its founder, Fritz Demopoulos).

Wave data were furnished by the Coastal Data Information Program (CDIP), Integrative Oceanography Division, operated by the Scripps Institution of Oceanography, under the sponsorship of the U.S. Army Corps of Engineers and the California Department of Parks and Recreation (`https://doi.org/10.18437/C7WC72`).

References

Abbott, I. A., & Hollenberg, G. J. (1992). *Marine algae of california*. Stanford University Press.

Dayton, P. K., Currie, V., Gerrodette, T., Keller, B. D., Rosenthal, R., & Tresca, D. V. (1984). Patch dynamics and stability of some california kelp communities. *Ecological Monographs*, *54*(3), 253–289. https://doi.org/10.2307/1942498

Dean, R. G., & Dalrymple, R. A. (1991). *Water wave mechanics for engineers and scientists* (Vol. 2). World Scientific Publishing Company. https://doi.org/10.1142/1232

Denny, M. W., Gaylord, B. P., & Cowen, E. A. (1997). Flow and flexibility ii. the roles of size and shape in determining wave forces on the bull kelp nereocystis luetkeana. *Journal of Experimental Biology*, *200*(24), 3165–3183. https://doi.org/10.1242/jeb.200.24.3165

Eger, A. M., Marzinelli, E. M., Beas-Luna, R., Blain, C. O., Blamey, L. K., Byrnes, J. E., ... others (2023). The value of ecosystem services in global marine kelp forests. *Nature Communications*, *14*(1), 1894. https://doi.org/10.1038/s41467-023-37385-0

Elwany, M. H. S., O'Reilly, W. C., Guza, R. T., & Flick, R. E. (1995). Effects of southern california kelp beds on waves. *Journal of Waterway, Port, Coastal, and Ocean Engineering*, *121*(2), 143–150. https://doi.org/10.1061/(ASCE)0733-950X(1995)121:2(143)

Frieder, C. A., Yan, C., Chamecki, M., Dauhajre, D., McWilliams, J. C., Infante, J., ... Davis, K. A. (2022). A macroalgal cultivation modeling system (macmods): evaluating the role of physical-biological coupling on nutrients and farm yield. *Frontiers in Marine Science*, *9*. https://doi.org/10.3389/fmars.2022.752951

Froehlich, H. E., Afflerbach, J. C., Frazier, M., & Halpern, B. S. (2019). Blue growth potential to mitigate climate change through seaweed offsetting. *Current Biology*, *29*(18), 3087–3093. https://doi.org/10.1016/j.cub.2019.07.041

Gao, G., Gao, L., Jiang, M., Jian, A., & He, L. (2021). The potential of seaweed cultivation to achieve carbon neutrality and mitigate deoxygenation and eutrophication. *Environmental Research Letters*, *17*(1), 014018. https://doi.org/10.1088/1748-9326/ac3fd9

Gaylord, B., Denny, M. W., & Koehl, M. A. (2003). Modulation of wave forces on kelp canopies by alongshore currents. *Limnology and Oceanography*, *48*(2), 860–871. https://doi.org/10.4319/lo.2003.48.2.0860

Gaylord, B., Rosman, J. H., Reed, D. C., Koseff, J. R., Fram, J., MacIntyre, S., . . . others (2007). Spatial patterns of flow and their modification within and around a giant kelp forest. *Limnology and Oceanography*, *52*(5), 1838–1852. https://doi.org/10.4319/lo.2007.52.5.1838

Henderson, S. M. (2019). Motion of buoyant, flexible aquatic vegetation under waves: simple theoretical models and parameterization of wave dissipation. *Coastal Engineering*, *152*, 103497. https://doi.org/10.1016/j.coastaleng.2019.04.009

Hoegh-Guldberg, O., Lovelock, C., Caldeira, K., Howard, J., Chopin, T., & Gaines, S. (2019). The ocean as a solution to climate change: five opportunities for action.

Jackson, G. A., & Winant, C. D. (1983). Effect of a kelp forest on coastal currents. *Continental Shelf Research*, *2*(1), 75–80. https://doi.org/10.1016/0278-4343(83)90023-7

Johnson, A. S., & Koehl, M. A. R. (1994). Maintenance of dynamic strain similarity and environmental stress factor in different flow habitats: thallus allometry and material properties of a giant kelp. *Journal of Experimental Biology*, *195*(1), 381–410. https://doi.org/10.1242/jeb.195.1.381

Journee, J., & Massie, W. (2000). *Offshore hydromechanics* (Vol. 1). CITG Section Hydraulic Engineering.

Kain, J. M., & Dawes, C. (1987). Useful european seaweeds: past hopes and present cultivation. *Hydrobiologia*, *151*, 173–181. https://doi.org/10.1007/BF00046124

Keulegan, G. H., & Carpenter, L. H. (1956). *Forces on cylinders and plates in an oscillating fluid*. National Bureau of Standards.

Lei, J., & Nepf, H. M. (2019). Wave damping by flexible vegetation: Connecting individual blade dynamics to the meadow scale. *Coastal Engineering*, *147*, 138–148. https://doi.org/10.1016/j.coastaleng.2019.01.008

Luhar, M., & Nepf, H. M. (2011). Flow-induced reconfiguration of buoyant and flexible aquatic vegetation. *Limnology and Oceanography*, *56*(6), 2003–2017. https://doi.org/10.4319/lo.2011.56.6.2003

Luhar, M., & Nepf, H. M. (2016). Wave-induced dynamics of flexible blades. *Journal of Fluids and Structures*, *61*, 20–41. https://doi.org/10.1016/j.jfluidstructs.2015.11.007

Marjoribanks, T. I., Hardy, R. J., Lane, S. N., & Parsons, D. R. (2014). High-resolution numerical modelling of flow—vegetation interactions. *Journal of Hydraulic Research*, *52*(6), 775–793. https://doi.org/10.1080/00221686.2014.948502

Milledge, J. J., Smith, B., Dyer, P. W., & Harvey, P. (2014). Macroalgae-derived biofuel: a review of methods of energy extraction from seaweed biomass. *Energies*, *7*(11), 7194–7222. https://doi.org/10.3390/en7117194

Monismith, S., Alnajjar, M., Daly, M., Valle-Levinson, A., Juarez, B., Fagundes, M., ... Woodson, C. B. (2022). Kelp forest drag coefficients derived from tidal flow data. *Estuaries and Coasts*, *45*(8), 2492–2503. https://doi.org/10.1007/s12237-022-01098-2

Mullarney, J. C., & Henderson, S. M. (2010). Wave-forced motion of submerged single-stem vegetation. *Journal of Geophysical Research: Oceans*, *115*(C12). https://doi.org/10.1029/2010JC006448

Mullarney, J. C., & Pilditch, C. A. (2017). The differential response of kelp to swell and infragravity wave motion. *Limnology and Oceanography*, *62*(6), 2524–2537. https://doi.org/10.1002/lno.10587

Nikora, V., Goring, D., & Biggs, B. (1998). A simple model of stream periphyton-flow interactions. *Oikos*, *81*, 607–611. https://doi.org/10.2307/3546782

Peteiro, C. (2018). Alginate production from marine macroalgae, with emphasis on kelp farming. *Alginates and Their Biomedical Applications*, *11*, 27–66. https://doi.org/10.1007/978-981-10-6910-9_2

Razmi, A. M., Chamecki, M., & Nepf, H. M. (2020). Efficient numerical representation of the impacts of flexible plant reconfiguration on canopy posture and hydrodynamic drag. *Journal of Hydraulic Research*, *58*(5), 755–766. https://doi.org/10.1080/00221686.2019.1671511

Rosman, J. H., Denny, M. W., Zeller, R. B., Monismith, S. G., & Koseff, J. R. (2013). Interaction of waves and currents with kelp forests (macrocystis pyrifera): Insights from a dynamically scaled laboratory model. *Limnology and Oceanography*, *58*(3), 790–802. https://doi.org/10.4319/lo.2013.58.3.0790

Sarpkaya, T., & O'Keefe, J. L. (1996). Oscillating flow about two and three-dimensional bilge keels. *Journal of Offshore Mechanics and Arctic Engineering*, *118*(1), 1–6. https://doi.org/10.1115/1.2828796

Schiel, D. R., & Foster, M. S. (2015). *The biology and ecology of giant kelp forests*. University of California Press.

Seymour, R., Tegner, M., Dayton, P., & Parnell, P. (1989). Storm wave induced mortality of giant kelp, macrocystis pyrifera, in southern california. *Estuarine, Coastal and Shelf Science*, *28*(3), 277–292. https://doi.org/10.1016/0272-7714(89)90018-8

Thornton, T. F. (2015). The ideology and practice of pacific herring cultivation among the tlingit and haida. *Human Ecology*, *43*, 213–223. https://doi.org/10.1007/s10745-015-9736-2

Utter, B. D., & Denny, M. W. (1996). Wave-induced forces on the giant kelp macrocystis pyrifera (agardh): field test of a computational model. *Journal of Experimental Biology*, *199*(12), 2645–2654. https://doi.org/10.1242/jeb.199.12.2645

Vogel, S. (1984). Drag and flexibility in sessile organisms. *American Zoologist*, *24*(1), 37–44. https://doi.org/10.1093/icb/24.1.37

Zeller, R. B., Weitzman, J. S., Abbett, M. E., Zarama, F. J., Fringer, O. B., & Koseff, J. R. (2014). Improved parameterization of seagrass blade dynamics and wave attenuation based on numerical and laboratory experiments. *Limnology and Oceanography*, *59*(1), 251–266. https://doi.org/10.4319/lo.2014.59.1.0251

Zhu, L., Zou, Q.-P., Huguenard, K., & Fredriksson, D. W. (2020). Mechanisms for the asymmetric motion of submerged aquatic vegetation in waves: a consistent-mass cable model. *Journal of Geophysical Research: Oceans*, *125*(2). https://doi.org/10.1029/2019JC015517

Supporting Information for "Wave-Induced Motion and Drag Reduction of Kelp"

Jayde F. Meng[1], Marcelo Chamecki[1]

[1]Department of Atmospheric and Oceanic Sciences, University of California, Los Angeles, CA 90025, USA

Contents of this file

1. Figure S1

Additional Supporting Information (Files uploaded separately)

1. Caption for large Table S1
2. Captions for Movies S1 to S4

Introduction

To support our discussion, we have included supplementary animations of the equilibrium cycles of kelp frond motion corresponding with Fig. 4 in the main text. In all movies, the black line represents the modeled kelp frond, blue dashed lines represent the wave excursion, and gray arrows represent the direction and relative magnitude of the instantaneous fluid velocity. Both axes are normalized by frond length (l). Frame rates are standardized across all animations so that each cycle appears 10 s long and is looped 5 times. Additionally, Figure S1 is included to help illustrate the relationship between the frond velocity and relative velocity between the flow and the frond. Table S1 lists all the variables and notation referenced in the main text.

Table S1. List of all variables referenced in the main text. Boldface denotes vector quantities.

Movie S1. Movie illustrating frond motion corresponding with Fig. 4a (buoyancy dominated), with $H_s = 0.25$ [m], $T_p = 20$ [s], $l = 2$ [m].

Movie S1. : Movie illustrating frond motion corresponding with Fig. 4b (drag dominated), with $H_s = 2$ [m], $T_p = 20$ [s], $l = 10$ [m].

Movie S1. : Movie illustrating frond motion corresponding with Fig. 4b (drag dominated), with $H_s = 0.25$ [m], $T_p = 5$ [s], $l = 10$ [m].

Movie S1. : Movie illustrating frond motion corresponding with Fig. 4b (drag dominated), with $H_s = 0.25$ [m], $T_p = 20$ [s], $l = 5$ [m].

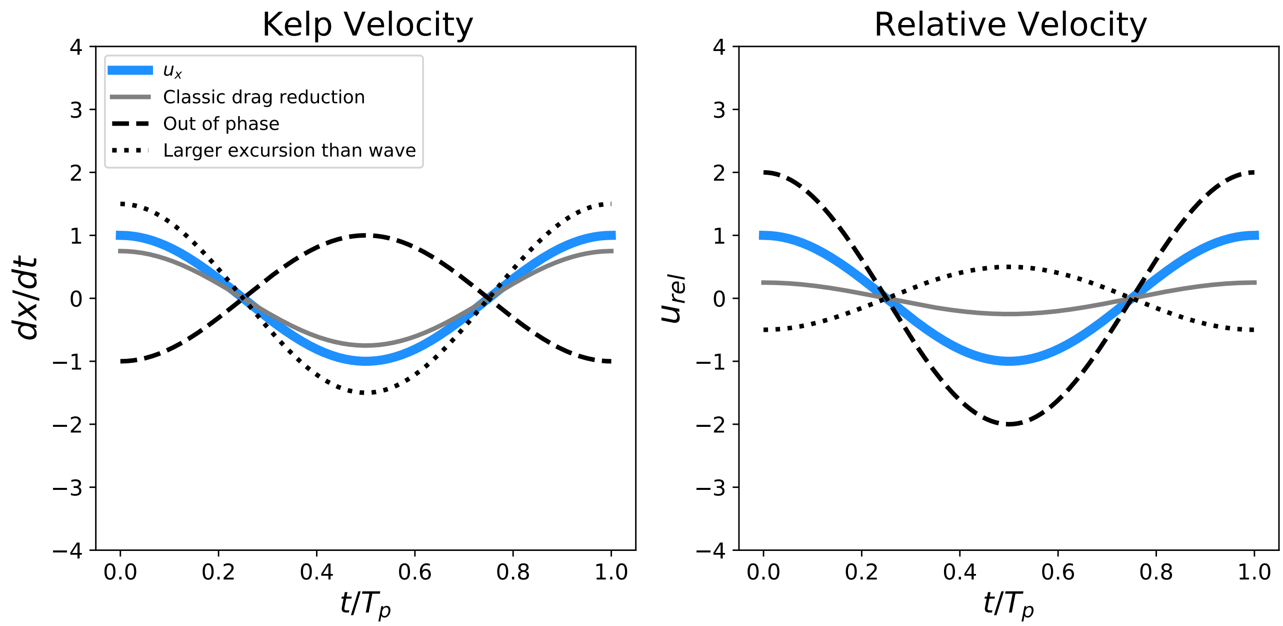

Figure S1. Schematic illustrating how different profiles of kelp frond velocity and their corresponding relative velocity plots. Thick blue lines represent the wave velocity; solid gray lines represent classical example of a flexible frond with reduced drag (e.g., the frond moves closely with the wave and thus has little relative velocity); dashed black lines represent a frond moving out of phase with the wave (e.g., Fig 7a); dotted black lines represent a frond with a larger excursion than the wave does (e.g., Fig 7b).

Variable	Description
β_{xT}	Parameter for asymmetric motion
δx	Relative horizontal blade excursion
$\delta x_w(z)$	Local horizontal wave excursion
Δt	Time step
Δx_w	Average horizontal wave excursion along length of kelp
ΔF	Parameter for ratio of top drag force and bottom drag force
γ	Ratio of frond length to wavelength
λ	Wavelength
ρ_k	Density of kelp
ρ_w	Density of seawater
θ	Angle of deflection from the vertical
ω	Wave frequency
a	Area per unit length
A	Maximal projected area of a frond
A_c	Cross-sectional area of a stipe
A_w	Wave amplitude
B	Buoyancy parameter
C_a	Added mass coefficient
C_d	Drag coefficient
$C_{d,f}$	Reduced drag coefficient
Ca	Cauchy number
d	Thickness of a plate
E	Modulus of elasticity
$\mathbf{e}_s$	Unit vector in direction of segment
$\mathbf{F}_{AM}$	Added mass force
$\mathbf{F}_B$	Buoyant force
$\mathbf{F}_D$	Drag force
F_D	Horizontal drag force
$F_{D,Rig}$	Rigid drag force

$F_{D,top}$	Top drag force
$F_{D,bot}$	Bottom drag force
$\mathbf{F}_P$	Pressure gradient force
$\mathbf{F}_T$	Tension force
$\mathbf{g}$	Gravitational acceleration vector
H	Depth of water column
H_s	Wave height
I	Second moment of area
k	Wavenumber
KC	Keulegan-Carpenter number
l	Frond length
l_e	Effective length
L	Ratio of blade length to wave excursion
M_A	Average mass per unit area
m_k	Effective mass of each segment
n	Number of segments
P	Ca/B
r_s	Radius of stipe
T_p	Wave period
$\mathbf{u} = (u_x, u_z)$	Fluid velocity
u_k	X-component of the kelp tip velocity
u_{rel}	Normalized relative velocity
U_w	Characteristic wave orbital velocity scale
V	Estimated volume of a frond
$\mathbf{x} = (x, z)$	Position vector of each point mass
$\bar{z}$	Mean vertical position of each segment over one wave cycle
$\mathbf{x}_i$	Denotes ith segment of kelp model
*	Denotes dimensionless and of order unity